JCI The Journal of Clinical Investigation

Endothelial C3a receptor mediates vascular inflammation and BBB permeability during aging

Nicholas E. Propson, Ethan R. Roy, Alexandra Litvinchuk, Jorg Köhl, Hui Zheng

J Clin Invest. 2020. https://doi.org/10.1172/JCI140966.

Research In-Press Preview **Aging**

Graphical abstract

Endothelial C3a receptor mediates vascular inflammation and BBB permeability during aging

Nicholas E. Propson[1,2], Ethan R. Roy[2], Alexandra Litvinchuk[2*], Jörg Köhl[3] and Hui Zheng[1,2,4**]

[1]Department of Molecular and Cell Biology, Baylor College of Medicine, Houston, TX, USA

[2]Huffington Center on Aging, Baylor College of Medicine, Houston, TX, USA

[3]Institute for Systemic Inflammation Research, Center for Infectiology and Inflammation Research Lübeck, University of Lübeck, Lübeck, Germany

[4]Department of Molecular and Human Genetics. Baylor College of Medicine, Houston, TX, USA

[*]Present address: Department of Neurology, Washington University School of Medicine, St. Louis, MO, USA

**Corresponding author: Hui Zheng, Huffington Center on Aging, Baylor College of Medicine, One Baylor Plaza, Houston, TX 77030. Phone: 713-798-1568. E-mail: huiz@bcm.edu)

The authors have declared that no conflict of interest exists.

Abstract

Dysfunction of immune and vascular systems has been implicated in aging and Alzheimer's disease; however, their interrelatedness remains poorly understood. The complement pathway is a well-established regulator of innate immunity in the brain. Here, we report robust age-dependent increases in vascular inflammation, peripheral lymphocyte infiltration, and blood-brain barrier (BBB) permeability. These phenotypes were subdued by global inactivation and by endothelial-specific ablation of *C3ar1*. Using an *in vitro* model of the BBB, we identify intracellular Ca^{2+} as a downstream effector of C3a-C3aR signaling and a functional mediator of VE-cadherins junction and barrier integrity. Endothelial *C3ar1* inactivation also dampened microglia reactivity and improved hippocampal and cortical volumes in the aging brain, demonstrating a crosstalk between brain vasculature dysfunction and immune cell activation and neurodegeneration. Further, prominent C3aR-dependent vascular inflammation is also observed in a tau transgenic mouse model. Our studies suggest that heightened C3a-C3aR signaling through endothelial cells promotes vascular inflammation and BBB dysfunction and contribute to overall neuroinflammation in aging and neurodegenerative disease.

Keywords: Aging; Blood-Brain Barrier; C3aR; Complement; Endothelial Cells; Peripheral Infiltration; Vasculature

Introduction

The natural aging process includes functional and structural changes within the brain (1, 2), and these changes have been shown to play a role in decreased neural stem cell fitness, altered cognition, and increased susceptibility for neurodegenerative disease (1, 3, 4). One such age-dependent change with potentially causal association to both normal decline and disease is dysfunction of the blood-brain barrier (BBB). The BBB is composed of endothelial cells, astrocytes, and pericytes, and an intact BBB is essential for brain health (5). Loss of vessel integrity is thought to drive BBB dysfunction, and can be found in numerous neurological disease conditions, namely traumatic brain injury (6), stroke (7), and often comorbidly in neurodegeneration (8). However, mechanisms controlling changes in brain vasculature and their consequence to CNS function, in particular during aging, remain ill-defined.

Recent work has demonstrated a vascular component to age-related changes in the brain, deterioration in cognition, and eventual dementia (9, 10). Furthermore, evidence that vascular inflammation, marked by increased endothelial expression of vascular cell adhesion molecule VCAM1, stokes CNS aging by decreasing neural stem cell number and increasing microglial reactivity has been reported (11). Elevated levels of VCAM1 have also been found to correlate with Parkinson's disease severity (12) and, recently, lymphocytes known to bind VCAM1 in brain vasculature were found in aged and AD patient brains (13, 14). Single-cell transcriptomic analysis of hippocampal brain endothelial cells (BECs) has shown that age-related changes in these cells are rooted in responses to innate inflammatory cues, hypoxic stimuli, and oxidative stress (15). Together, these studies suggest a significant inflammatory transition in brain vasculature with age and the potential for causal connection to CNS diseases.

While studies of blood plasma components have implicated circulating factors in maintaining or diminishing brain health during aging (16), others exploring local inflammatory cues in the CNS have highlighted the inherent capacity of glia to modulate neuroinflammation (17).

One of the primary innate immune signaling mechanisms involved in neuroinflammation is the complement pathway. Complement components are expressed by cells of the CNS and are reported to influence CNS aging and neurodegenerative disease progression (18). In particular, complement component C3 is capable of potentiating age-related and neurodegenerative changes in the CNS (19-22). The active signaling peptide of C3, C3a, is released via cleavage by the extracellular enzyme C3 convertase. Once cleaved, C3a signals through its cognate receptor C3aR, which has been detected on microglia (23), choroid plexus epithelium (24) , and vascular endothelial cells (25) in the brain. C3 is upregulated in astrocytes during aging and disease (22, 26), and the intimate relationship of astrocytes with the BBB supports the premise that C3 produced by these cells may play a direct role in age-related changes in brain vasculature.

Using *in vivo* and *in vitro* models we identify a mechanism by which the C3a-C3aR signaling axis modulates VCAM1 expression, influences peripheral immune cell infiltration, alters vascular morphology, increases BBB permeability, and potentiates microglial reactivity and neurodegeneration in aged mice. We further show that this C3aR-dependent endothelial phenotype is exacerbated in PS19 tau transgenic mice, a model in which elevated C3-C3aR signaling was shown to modulate CNS inflammation and tau pathology (22). This study identifies complement signaling as a key mediator of vascular dysfunction in brain aging and disease.

Results

C3a-C3aR signaling regulates age-associated endothelial VCAM1 expression and immune cell infiltration

C3 mRNA has been shown to be upregulated in aged astrocytes (20, 26). To corroborate this finding, we measured C3 protein in lysates of mouse brains at 2, 12, and 20 months of age by ELISA. We detected a significant increase at 12 months, with a further increase at 20 months, over levels detected in the young mice (Figure 1A). Consistent with our earlier reports in disease models (21, 22), co-immunofluorescent labelling of the hippocampus showed C3 expression

predominantly colocalized in GFAP$^+$ astrocytes where its levels were elevated during aging (Figure 1, B and C, Supplemental Figure 1A). Increased *C3* mRNA was further validated in FACS-sorted aged astrocytes using our previously published method (27) (Supplemental Figure 1B). To examine the expression of C3aR in brain vasculature, we isolated vessels from wild-type and *C3ar1*$^{-/-}$ mouse brains (28), and immunostained them with antibodies against GFAP, VE-cadherin, and C3aR. Positive C3aR staining can be readily detected in VE-cadherin$^+$ BECs in wild-type, but not *C3ar1*$^{-/-}$ vessels (Figure 1D). High resolution confocal imaging analysis of CD31, Glut1, and C3aR on mouse brain vasculature revealed a greater polarization of C3aR toward the basolateral surface whereas Glut1 localized predominantly toward the vessel lumen (Figure 1E, Supplemental Figure 1C). In contrast to the endothelial expression, co-staining for C3aR and the pericyte marker PDGFRβ did not detect appreciable colocalization (Figure 1E). Flow cytometry analysis of human brain microvascular endothelial cells (HBMECs) showed high levels of positivity for VE-Cadherin (80.9%) and Glut1 (94.2%) as expected, and this positivity was also observed for C3aR although to a lesser degree (34.3%) (Supplemental Figure 1D). Together, these results establish C3aR expression in brain vascular endothelial cells and support a signaling axis involving astroglial C3 and endothelial C3aR at the BBB.

To assess the functional role of this signaling pathway, we first analyzed the expression of VCAM1, as it has been implicated in complement-mediated activation of BECs in both LPS-induced neuroinflammation (29) and ischemia models (30). Co-immunofluorescent labelling of brain cortical vasculature revealed that VCAM1 expression was restricted to CD31$^+$ vasculature, where its levels were increased with age in wild-type mice, but not in *C3ar1* null mice (Figure 1, F and G). A similar reduction in vascular VCAM1 was also seen after treating 2-, 12-, and 20-month-old mice with the C3aR antagonist (C3aRA) SB290157 (Supplemental Figure 2, A and B), further confirming our genetic study and validating the inhibitory effect of the C3aRA. The same is true when hippocampal samples were analyzed (Supplemental Figure 2C). We then performed deeper analysis by measuring *Vcam1* mRNA levels in FACS-sorted mouse BECs from 2-, 12-,

and 20-month-old cohorts treated with vehicle or C3aRA, which showed increased *Vcam1* expression with age in vehicle treated samples, but blunted expression with C3aRA treatment (Supplemental Figure 2D).

To substantiate this signaling pathway in human cells and to test a direct effect of C3a-C3aR signaling, we treated primary HBMECs with recombinant human C3a, with or without C3aRA, and found a robust increase in *Vcam1* expression by C3a treatment, which was quelled in the presence of C3aRA (Supplemental Figure 2E). Interestingly, other adhesion molecules, namely *Sele* and *Icam1*, were not significantly changed by this treatment (Supplemental Figure 2, F and G). Additionally, similar ICAM1 immunointensities (Supplemental Figure 2, H-J) and *Icam1* mRNA levels (Supplemental Figure 2K) were detected in 2- and 20-month-old mouse brains. Together, these data support both the necessity and sufficiency of C3a signaling in modulating VCAM1 expression in brain endothelial cells.

Next, we examined the functional consequence of C3-mediated VCAM1 upregulation. It has been previously shown that increased numbers of peripheral lymphocytes are found in the aged brain (31) and reside in the neural stem cell niche of the subventricular zone (13). Since adhesion molecules regulate the process of rolling adhesion and extravasation of immune cells, we hypothesized that increased brain VCAM1 expression in vasculature during aging may be associated with increased peripheral immune cell infiltration. Using FACS to discriminate $CD45^{hi}/CD11b^{-}$ lymphocytes (LY) from $CD45^{hi/mid}/CD11b^{+}$ monocytes (MN) and microglia (MG) in dissociated brain tissues, we found increasing proportions of $CD45^{hi}/CD11b^{-}$ infiltrates at 12 and 20 months compared to 2-month-old controls (Figure 2, A and B). In contrast, monocytes were not significantly changed with age (Supplemental Figure 3A). We next asked whether, in addition to reducing VCAM1 expression levels, blocking C3aR signaling could reduce age-related lymphocyte infiltration. Flow cytometry analysis of 12- to 14-month-old *C3ar1*$^{-/-}$ mice revealed a reduction in the total percentage of $CD45^{hi}/CD11b^{-}$ infiltrating lymphocytes in the brain compared to wild-type controls (Figure 2, C and D), while monocytes were unaffected (Supplemental Figure

3B). Similar reductions in $CD45^{hi}/CD11b^{-}$ infiltrating lymphocytes but not monocytes were observed after treating 20-month-old wild-type mice with C3aRA (Supplemental Figure 3, C-E).

Since acute neuroinflammation induces peripheral immune cell infiltration (29), we tested the role of C3aR in recruiting these cells following intracerebroventricular (i.c.v.) administration of LPS in 3- to 4-month-old wild-type and *C3ar1*$^{-/-}$ mice (Supplemental Figure 4A). As expected, LPS challenge led to increased lymphocyte (Supplemental Figure 4B) and monocyte (Supplemental Figure 4C) infiltration in the brains of wild-type mice. In contrast, genetic ablation of *C3ar1* blunted the infiltration of $CD45^{hi}/CD11b^{-}$ peripheral lymphocytes (Supplemental Figure 4B) while monocyte cell numbers were only marginally affected (Supplemental Figure 4C). Consistent with the specific regulation of VCAM1 by C3a-C3aR signaling, deletion of *C3ar1* significantly suppressed *Vcam1* gene expression induced by LPS without affecting *Sele* and *Icam1* in FACS-sorted BECs (Supplemental Figure 4D).

To access whether the LPS-induced acute neuroinflammation affects BBB permeability, we analyzed each group using a tail-vein injection of a BBB impenetrable TRITC-Dextran dye (65-85 kDa). Interestingly there was no significant increase in BBB permeability under acute neuroinflammatory stimuli that contributed to this infiltration event (Supplemental Figure 4E). To confirm the induction of neuroinflammation by LPS, we analyzed sorted microglia from the vehicle and LPS treated animals and found consistent microglial gene response signatures as we have previously reported (27) (Supplemental Figure 4F).

Together these results suggest that C3a acts through endothelial C3aR to promote VCAM1 expression, and that during both aging and acute neuroinflammation, this pathway plays a role in selective infiltration of lymphocytes into the brain.

$CD8^{+}$ T cells preferentially infiltrate the aged brain

We next examined the lymphocyte sub-types infiltrating the aged brain and compared these with the cells of the aged spleen to better understand the global changes to lymphocyte composition

in aged tissues. Dissociated cells from 20-month-old wild-type brain or spleen were immunostained using anti-CD45, anti-CD11b, anti-CD3ε, anti-CD19, anti-CD8a, and anti-CD4 antibodies. Following antibody staining cells were analyzed by flow cytometry to differentiate monocytes (MN), microglia (MG), and lymphocytes (LY) (Figure 3A, left panels). Further subtyping was carried out analyzing T-lymphocyte (TC) vs. B-lymphocyte (BC) composition (Figure 3A, middle panels), and T-lymphocyte subtyping to differentiate $CD8^+$ vs. $CD4^+$ T cells (Figure 3A, right panels). In 20-month-old wild-type mice, we found infiltrating lymphocytes were predominantly $CD3^+$ (75%) vs. $CD19^+$ (10%), while analysis of matched spleens showed significantly more $CD19^+$ (65%) cells vs. $CD3^+$ (25%) cells (Figure 3B), suggesting that the aged brain preferentially recruits $CD3^+$ T cells compared to aged spleen. Further analysis of brain $CD3^+$ T cells showed that the majority were $CD8^+$ T cells (75%) instead of $CD4^+$ T cells (15%), which also inversely correlated with the peripheral splenic tissue where $CD4^+$ T cells were significantly more abundant than $CD8^+$ T cells (Figure 3C). This data suggests that $CD8^+$ T cells are preferentially recruited to the aged brain compared to other lymphocyte subsets.

To further evaluate whether this age-dependent change was specific to brain parenchyma representing potential infiltration we isolated the choroid plexus tissue from brain ventricles of 2- and 20-month-old mice prior to dissociation, using the spleen as a control, and performed similar analyses as stated above. Using the same flow cytometry gating strategy, we saw increased numbers of $CD3^+$ and $CD8^+$ lymphocytes only in aged brains, but not in aged choroid plexus tissue (Supplemental Figure 5, A-C) or spleen (Supplemental Figure 5, D-F). These data suggest that age-related $CD8^+$ lymphocyte infiltration is specific to brain parenchyma, and not present in other immune cell rich regions of the brain or peripheral tissues.

To confirm that peripheral cells are recruited and infiltrate into the aged brain, we employed an mT/mG reporter mouse model which produces tdTomato under the *ROSA26* locus (32). When crossed with Mx1-Cre mice and activated by peripheral poly I:C (polyinosinic:polycytidylic acid) treatment, Cre-responsive cells in the periphery recombine to

express EGFP, generating a chimeric mouse (MXG) (Supplemental Figure 6A). Analysis of peripheral blood mononuclear cells (PBMCs) confirmed that approximately 40% of PBMCs were converted to express EGFP in MXG mice (Supplemental Figure 6, B-D). To assess brain infiltration of $EGFP^+$ peripheral cells during aging, we injected mice with poly I:C at 2 months of age and allowed mice to age to 15 months. Flow cytometry analysis of dissociated brains showed approximately half of infiltrating $CD45^{hi}/CD11b^-$ lymphocytes expressed EGFP in 15-month-old MXG brains (Supplemental Figure 6, E-G), demonstrating that lymphocytes in aged brains are peripherally derived. Confocal imaging of the aged brain tissue confirmed the presence of $EGFP^+$ infiltrated peripheral immune cells along the basolateral surface of $tdTomato^+EGFP^-$ brain vessels, further indicating the peripheral origin of the cells (Supplemental Figure 6H).

To better understand the regional distribution of these $CD8^+$ infiltrates we analyzed 2- and 20-month-old mouse brain tissue by immunostaining with antibodies against CD8 to mark the T cells of interest and Col IV to mark the endothelial basement membrane (Figure 3, D and E). Besides the SVZ as previously reported (13), it was clear that CD8 T cells were present in other brain regions as well. Notably, the cortex (CTX), thalamus (THAL), caudate putamen (CPu), and the hippocampus (HPC), all had a significant presence of CD8 T cells with age (Figure 3F). These cells were found either residing along the basolateral surface with colocalized Col IV (Figure 3G left panel), extravasating with minimally colocalized Col IV (Figure 3G middle panel), or fully extravasated into the tissue parenchyma (Figure 3G right panel). Overall, these findings demonstrate that during aging peripherally derived $CD8^+$ T cells preferentially infiltrate and take up residence inside the brain parenchyma in numerous tissue regions.

Inhibition of C3aR rescues age-related changes in vascular morphology and BBB permeability

We next determined the effect of C3a-C3aR signaling on brain vascular morphology at different ages. We performed confocal imaging and 3D reconstruction of the vasculature, visualized by

collagen IV (Col IV) staining, and measured the average cross-sectional area of hippocampal capillaries by dividing the total Col IV$^+$ volume by the total capillary length in each reconstructed image. Capillaries in young mice showed an average cross-sectional area of ~60 μm^2, whereas capillaries in 12- and 20-month-old mice averaged ~40 μm^2 (Figure 4A). This reduction was partially, but significantly, rescued in 20-month-old aged *C3ar1*$^{-/-}$ mice, and in mice treated with the C3aRA (Figure 4B). Analysis of each component of this measurement demonstrates a decrease in total vascular volume (Supplemental Figure 7A) and an increase in vessel length (Supplemental Figure 7B) during aging, both of which contribute to decreased average cross-sectional area. Additionally, CD31$^+$ vessels showed a higher degree of tortuosity in the aged hippocampus, as previously defined by their corkscrew-like morphology (33, 34) (Figure 4C, marked by rectangles). This phenomenon has been linked to decreased hemodynamic flow and hypoxia in affected brain regions (33, 34). The overall incidence of tortuous vessel segments was increased ~2- and ~4-fold by 12 and 20 months, respectively, over that observed in 2-month-old mice (Figure 4, C and D). This vascular phenotype was rescued by both genetic ablation of *C3ar1* and C3aRA treatment in 20-month-old mice (Figure 4, C and D). Thus, blocking C3aR significantly improves vascular morphology in aged mice.

Given the observed age-associated changes in lymphocyte infiltration and vascular morphology, we tested whether BBB integrity was affected by C3a-C3aR signaling. We used a previously reported method allowing detection of peripherally-administered fluorescent dextran leakage into the brain (35) (Figure 4E). At 2 months there was almost no detection of fluorescent dextran in brain tissues, while there was a robust increase in fluorescent signal in 20-month-old brains, localized around lectin$^+$ vasculature (Figure 4E). Quantification of dextran levels in brain homogenates of 2-, 12-, and 20-month-old mice showed an age-dependent tracer leakage into the brain at 12 months (~2 fold) and 20 months (~3-fold) (Figure 4F). Treating 20-month-old mice with C3aRA modestly, but significantly, reduced tracer leakage (Figure 4G).

To further characterize age-associated changes of BBB integrity, we examined VE-cadherin^{+} intercellular junctions by confocal microscopy in vessels isolated from 2-, 12-, and 20-month-old mouse brains (28), with or without C3aRA treatment (Figure 4H and Supplemental Figure 7C). Quantification of immunoreactivity in both large vessels (Figure 4I) and capillaries (Supplemental Figure 7D) revealed age-associated downregulation of VE-cadherin, with modest but significant rescue by C3aRA treatment. Consistent with this, gene expression analysis of FACS-sorted brain endothelial cells showed age-dependent reduction of *Cdh5* (encoding VE-cadherin) at 12 and 20 months, along with reductions in *Ocln*, *Tjp1*, and *Cldn5* mRNAs (Supplemental Figure 7E), reflecting impaired expression of junctional components. These age-dependent reductions were either trending or significantly restored with C3aRA treatment (Supplemental Figure 7E). Together these data suggest that C3aR inhibition partially restores BBB integrity in aged brains.

C3a-mediated barrier disruption involves Ca^{2+} mobilization, cytoskeletal activation, and VE-Cadherin disruption

To elucidate the mechanism of C3a-mediated BBB permeability *in vitro* we employed the use of trans-endothelial electrical resistance (TEER) measurements. Using chopstick electrodes and an EVOM2 ohmmeter to measure the resistance of electrical current in an isolated system, we could directly test the effect of various molecules in an *in vitro* barrier model (Figure 5A). Our model contained a co-culture of primary human astrocytes (HAsts) cultured for 2 days on the abluminal surface of a semi-permeable membrane prior to the addition of HBMECs, which were cultured on the luminal surface for another 4 days, while TEER was monitored for optimal resistance prior to beginning treatment. We first validated the capability of this system to generate a reproducible barrier. Using the TEER as a readout, we compared resistance of a cell-free membrane to barriers formed by primary astrocytes or endothelial cells, or by endothelial cells co-cultured with HeLa cells or primary astrocytes. We found that endothelial cells co-cultured with astrocytes, but not

with HeLa cells, significantly increased TEER (Supplemental Figure 8, A and B), demonstrating that astrocytes promote BBB integrity *in vitro*.

To test the effect of C3aR signaling we treated human endothelial-astrocyte co-cultures with recombinant human C3a, and used IL-1β treatment, known to disrupt barrier integrity, as a positive control (36). After a 24-hour treatment we found that C3a treatment resulted in a significant reduction of TEER, similar to IL-1β (Figure 5, B and C). C5a treatment had a marginal, but not statistically significant effect (Supplemental Figure 8, C and D). C3a-induced barrier dysfunction was blocked when cultures were co-treated with C3aRA (Figure 5, B and C).

To further elucidate the mechanism of C3aR-mediated BBB permeability we interrogated intracellular Ca^{2+} as a potential second messenger, given previous reports that activation of C3aR triggers Ca^{2+} release (37). Treating the co-cultures with ionomycin resulted in a drastic reduction of TEER (Supplemental Figure 8, E and F), suggesting Ca^{2+} release is sufficient to increase barrier permeability. Co-treatment with C3a and the calcium chelator BAPTA-AM, to block Ca^{2+} signaling, led to a rescue of C3a-mediated TEER reduction to the level observed with C3aRA intervention (Figure 5, D and E), suggesting that calcium release is the primary mechanism of barrier permeability downstream of C3a-C3aR signaling.

Next, we aimed to dissect the connection between changes in VE-Cadherin and Ca^{2+} that may result in increased barrier permeability downstream of C3aR activation. Previous work has shown that various endothelial cell lines respond to C3a by forming actin stress fibers within the cell (25). Following activation of the calcium-dependent kinase calmodulin, myosin light chain kinase is able to phosphorylate myosin light chain (MLC) motor protein at Ser19 (pMLC) resulting in stress fiber formation (38). Activation of this pathway is known to initiate a physical, tensile stress at the cell membrane, disrupting VE-Cadherin^{+} junctions and BBB integrity (39). Therefore, we hypothesized that C3a might trigger the calcium release needed to disrupt VE-Cadherin^{+} junctions resulting in BBB permeability.

To test this hypothesis, we treated endothelial cell monolayers with C3a alone or together with C3aRA, BAPTA-AM, or calmodulin inhibitor W7. Immunofluorescence staining of cells treated with C3a alone for 2 hrs showed a robust increase in both phalloidin^{+} F-actin stress fibers and overlapping pMLC signal (Supplemental Figure 9A). To quantify the dynamics of this cellular response, we analyzed changes at 2 hours, during the downward slope of barrier integrity, as measured by TEER analysis, following C3a stimulation. We saw a robust increase in pMLC by both immunofluorescence (Figure 5, F and G) and immunoblotting (Supplemental Figure 9, B and C), both of which were blocked by C3aRA, BAPTA, or W7 treatment. When analyzing the effect on VE-Cadherin we did not see overt changes by either immunofluorescence (Figure 5, F and G) or by immunoblotting (Supplemental Figure 9, B and D) under all conditions, suggesting that F-actin stress fiber formation and activation of pMLC, but not VE-Cadherin protein alteration, is involved in the early phase of C3a-C3aR signaling. However, following 24 hours of C3a treatment, pMLC levels normalized but VE-Cadherin levels were significantly reduced by both immunofluorescence staining (Figure 5, H and I) and by immunoblotting (Supplemental Figure 9, E and G). Co-treatment with C3aRA, BAPTA, or W7 normalized VE-Cadherin without affecting pMLC (Figure 5I, Supplemental Figure 9, E-G).

Overall, these data establish intracellular Ca^{2+} as a second messenger downstream of C3a-C3aR signaling to mediate pMLC activity and VE-Cadherin homeostasis in endothelial cells. These findings suggest that there are two phases in endothelial response to C3a. First a transient phase (2 hr) where endothelial cells respond quickly and rapidly to C3a signaling by forming stress fibers, followed by a failed ability to maintain VE-Cadherin protein levels leading to barrier permeability (24 hr).

Endothelial-specific deletion of *C3ar1* rescues vascular phenotypes, reduces microglial reactivity, and corrects age-related neurodegeneration

As *C3ar1* genetic ablation and C3aR pharmacologic inhibition were able to rescue age-related changes in brain vasculature, we hypothesized that specific endothelial ablation would show similar effects as global targeting, and that such a manipulation would influence age-related neuroinflammation overall. The above *in vitro* studies support a role of endothelial C3aR in mediating the barrier permeability. To test this hypothesis directly, we produced mice with conditional deletion of *C3ar1* in endothelial cells by crossing a *C3ar1* floxed allele (40) with the *Tie2-Cre (41)* mice to generate *C3ar1*$^{fl/fl}$*;Tie2-Cre* (T2KO) mice. Littermate *C3ar1*$^{+/+}$ and *C3ar1*$^{fl/fl}$ mice were used as controls (CTRL). The cell-type specific knockout was confirmed by immunofluorescent imaging (Supplemental Figure 10A).

Co-immunofluorescent staining of CTRL and T2KO mice at 3 and 12-14 months of age with anti-VCAM1 and anti-CD31 antibodies revealed significant increases in cortical vascular VCAM1 signal at 12-14 months of age in the CTRL group (Figure 6A). Similar to the germline deletion, age-associated elevation of VCAM1 expression was almost completely attenuated in the T2KO mice (Figure 6, A and B), which was also seen in hippocampus (Supplemental Figure 10, B and C). Analysis of vessel morphology by CD31 staining and 3D reconstruction showed a significant reduction in vessel cross sectional area in 12-14-month-old CTRL mice compared to that of 3-month-old mice (Figure 6, C and D). Consistent with the VCAM1 staining, endothelial deletion of *C3ar1* was sufficient to rescue the age-associated changes of vessel morphology (Figure 6, C and D). These data demonstrate that specifically ablating *C3ar1* in endothelial cells rescues age-related changes in brain vasculature similar to the global ablation and pharmacological inactivation. Thus, endothelial C3aR plays a cell-autonomous role in mediating age-dependent changes of vascular inflammation and morphology.

It was previously reported that reducing VCAM1 expression in endothelial cells can benefit brain function (11). Thus, we tested whether inhibiting the C3aR-VCAM1 axis at the endothelial cells could influence microglial reactivity. Co-immunostaining of 2- and 12-month-old wild-type and *C3ar1*$^{-/-}$ mice with microglia marker IBA1 and a marker for phagocytic microglia, CD68,

followed by colocalization analysis identified higher percentage of CD68 signal colocalized with IBA1 in 12-month-old wild-type mice, which was completely normalized by global C3aR inactivation (Figure 7, A and B). Analysis of T2KO mice and their littermate controls at 12-14 months showed a partial but significant reduction of CD68 immunoreactivity (Figure 7, C and D). This result suggests that although C3aR is expressed in other cell types, notably microglia, it also plays a role in mediating neuroinflammation in the brain by modulating the endothelial C3aR - VCAM1 axis and promoting peripheral immune cell interaction at the brain vasculature.

To determine whether the changes of immune cells detected in the middle age (12-14M) may lead to neuronal loss later in life, we performed Nissl staining of brain sections from young (3M) and old (20M) wild-type CTRL mice and 20M *C3ar1*$^{-/-}$ and T2KO mice (Supplemental Figure 11) and quantified hippocampal and piriform/entorhinal cortical volumes (Figure 7, E and F). We found a mild, but significant reduction in tissue volumes with age in the control animals. Interestingly, global and endothelial-specific ablation of C3aR lead to the comparable degree of rescue (Figure 7, E and F). Together these data suggest that blocking the endothelial C3aR-VCAM1 axis and restoring endothelial vascular morphology can both restore microglial function and restore brain health during aging.

C3aR modulates vascular changes in PS19 tau transgenic mice

Our previous analysis of the widely used PS19 tau transgenic mouse model reported heightened C3-C3aR signaling associated with hyperphosphorylated tau pathology, such that genetic deletion of *C3ar1* effectively reduced tau pathology and neuroinflammation (22). Examination of the previously reported brain transcriptomes of PS19 and PS19;*C3ar1*$^{-/-}$ mice (22) clearly demonstrated the capacity for C3aR to modulate the innate immune response. Further, overrepresentation analysis of this gene expression data, found KEGG and Reactome pathways upregulated in PS19 and downregulated in PS19;*C3ar1*$^{-/-}$ consistent with cytokine activation, leukocyte activation and migration, cell adhesion molecule interactions, and regulation or

activation of the cytoskeleton; all of which are consistent with endothelial responses to C3a (Figure 8A). In addition to leukocyte transcripts in our pathway analysis, specific transcripts identifying peripheral immune cell infiltration (*Vcam1, Ptpn22, Cd3e*, and *Cd8a*) were also significantly elevated in PS19 brains (Figure 8A, Supplemental Figure 12).

Given the changes in endothelial processes, and peripheral immune cell response, we hypothesized that the elevated C3a-C3aR-VCAM1 pathway contributes to vascular changes in PS19 mice. Indeed, co-immunofluorescent analysis of cortical vasculature of 9-month-old PS19 mice labelled with CD31 and VCAM1 revealed a significant increase in VCAM1 expression colocalized with $CD31^+$ vasculature, and this phenotype was rescued to control levels by ablating *C3ar1* (Figure 8, B and C). Increased VCAM1 expression in PS19 mice was accompanied by drastic reduction in the average cross-sectional area of cortical brain vasculature (Figure 8, D and E). Consistent with aging analysis, *C3ar1* ablation in PS19 animals significantly improved vascular morphology (Figure 8, D and E). These data reveal a novel vascular phenotype associated with tau pathology and suggest that the endothelial C3aR-VCAM1 axis contributes to vascular dysfunction in tauopathy.

Discussion

Our data provide evidence that activated C3a-C3aR signaling in brain endothelial cells triggers an increase in cell adhesion molecule VCAM1 and initiates an inflammatory transition affecting brain vascular structure and function during aging. This is associated with lymphocyte infiltration, altered vascular morphology, increased BBB permeability, and ultimately age-related neurodegeneration. Genetic or pharmacological C3aR inhibition rescues these age-associated phenotypes. Our *in vitro* BBB model implicates endothelial C3aR in the barrier disruption, and downstream intracellular Ca^{2+} signaling and VE-Cadherin localization and expression as the underlying mechanisms. A cell autonomous effect of endothelial C3aR is further validated by our demonstration that endothelial-specific ablation of *C3ar1* phenocopies germline deletion with

regard to vascular phenotypes. Analysis of the endothelial-specific *C3ar1* knockout mice also supports the notion that morphological and functional changes in vasculature contribute to microglial reactivity and age-related neurodegeneration. Finally, we document that similar vascular phenotypes and their C3aR dependency are observed in PS19 tau transgenic mice, supporting a common C3a-C3aR-VCAM1 signaling pathway in mediating neuroinflammation in aging and neurodegenerative disease.

To determine the functional consequence of the activated endothelial C3a-C3aR axis during aging, we analyzed VCAM1 expression and peripheral immune cell infiltration in the brain and found a substantial increase in $CD8^+$ T cells, whereas genetic and pharmacologic inhibition of the C3a-C3aR pathway reduced these phenotypes. This likely occurs through a VCAM1-regulated manner, since the interaction of vascular VCAM1 and its lymphocyte-expressed ligand VLA-4 is well established (42). These findings point toward a strong shift toward vascular inflammation in brain endothelial cells during aging.

A recent report by Yousef et al. concluded that elevated brain VCAM1 expression activated microglia and decreased neural stem cell number in aged mice (11). They also addressed the peripheral immune cell contribution by using αVLA-4 blocking antibodies in 16-month-old mice, showing a rescue of these phenotypes. Work by Dulken et al. also suggested that increased prevalence of clonally expanded $CD8^+$ T cells in the brains of 28-29-month-old mice significantly hindered neural stem cell fitness in the subventricular zone (13). These findings, along with ours, support a model of periodic immune cell infiltration and eventual clonal expansion during aging. Our C3aR inhibition studies and the VLA-4 blockade by Yousef et al. suggest blocking peripheral immune cell recruitment during aging may reduce microglial reactivity and dampen the activated neuroimmune environment, whereas allowing this to go unchecked in old mice results in further $CD8^+$ T cell infiltration and clonal expansion (of both early and late recruits). The partial rescue of infiltration in our 20-month-old pharmacologic inhibition model supports this supposition of periodic, age-dependent waves of infiltration. Though our study does not address

neural stem cell fitness or fate, we did show a C3aR-dependent effect on age-related neurodegeneration in our *C3ar1* null and T2KO mouse models. Together the current findings suggest that, in part, age-related neurodegeneration might be provoked by peripheral immune cell interaction with or signaling to microglia. Future studies should analyze more time points specifically in later stage of life to determine the exact windows of infiltration that affect brain function, and clearly identify the role of these $CD8^+$ T cell infiltrates. Recent work by Kolev et al. showed that peripheral immune cells elevate intrinsic C3 production following diapedesis into peripheral tissues (43). They suggest a prominent role for the $CD4^+$ T cell interaction (via LFA-1) with endothelia (via ICAM1), but also identify a similar effect in $CD8^+$ T cells stimulated with VCAM1, showing intrinsic upregulation of IFN-γ and C3 (43). Further dissecting this mechanism with respect to CD8+ T cells and VCAM1 could shed light on potential feed-forward mechanisms affecting microglial reactivity during aging.

We also analyzed structural and morphological characteristics of brain vasculature in the hippocampus, as this region was previously reported to undergo age-related vascular dysfunction in the form of BBB disruption and reduced cerebral blood flow (CBF) (44, 45). We found that C3a-C3aR signaling induced structural changes in vasculature affecting vessel cross sectional area and vessel tortuosity, characteristics previously associated with impaired CBF and abnormal angiogenesis (34). Additional work is needed to understand the exact impact of C3a on hemodynamics. Work by the Zlokovic group has shown that the BBB undergoes aged-related permeability in the hippocampus prior to disease (10, 44-46). We found that aged mouse brain vessels were more permeable to a BBB impenetrable tracer dye and confirmed the loss of barrier integrity by analyzing FACS-isolated endothelial cells, which showed impaired gene expression of critical BBB genes (*Cdh5*, *Ocln*, *Tjp1*, and *Cldn5*). Our data shows that C3a-C3aR signaling is partly responsible for these structural and functional changes in BBB integrity during aging.

Our data using dextran indicate that the immune cell infiltration by acute LPS treatment is an active process rather than the result of compromised BBB. This interpretation differs from a

previous report using heavy isotope and radio-labeled proteins, which revealed increased BBB permeability by LPS induction (47). While the exact cause for this discrepancy is not clear, recent work from the Wyss-Coray lab identified novel, age-related receptor-mediated transcytosis mechanisms for protein transfer across the BBB (48). It is possible that a similar transcytosis mechanism could underlie the presence of heavy isotope or radio-labeled proteins in the brain of acute neuroinflammatory models. Given this new development, further work should be done to better understand BBB permeability in acute neuroinflammation.

Mechanistic analysis of the endothelial barrier phenotype suggests a role for calcium-mediated signaling in an *in vitro* model of the BBB. Further analysis identified a potential phase response where initial calcium-mediated signaling induces phosphorylation of myosin light chain protein resulting in VE-cadherin protein loss at intercellular junctions. These effects were rescued by inhibition of C3aR or calmodulin in endothelial cell cultures, establishing a strong link between C3a-C3aR activation and calcium-mediated effects in brain endothelial cells. Together, these findings show that changes in brain vessel structure, hemodynamics, and BBB permeability may be directly modulated by glial reactivity and other complement-related changes seen in aged brains.

The major focus of this study addresses the role of age-related vascular changes due to C3a-C3aR signaling; however, we observed similar activation in the PS19 model of tauopathy. In our previous study of this model (22), we identified a key C3aR-dependent microglial activation network, and showed that blocking C3aR corrected microglial activation and other transcriptional changes. Activation of the C3a-C3aR network also influenced gene expression signatures consistent with peripheral immune cell activation, a phenomenon previously reported in other AD mouse models (49, 50). Given this, we reasoned that impaired vasculature and endothelial cell response may be partly responsible for the presence of peripheral immune cell signatures. Indeed, RNA-seq analysis revealed increased levels of *Vcam1, Cd3e, Cd8a,* and *Ptpn22* genes in PS19 hippocampi, and histology revealed highly altered vessel morphology. Previous work by

Faraco et al. demonstrated a role of hypertension in potentiating accumulation of hyperphosphorylated tau, a finding which corroborates our belief that endothelial structure and function may influence disease pathogenesis (51). The study by Laurent et al. used a CD3 T cell depletion strategy showing that *Clec7a, Itgax, Cd68,* and even astrocytic *Gfap* mRNA levels are reduced by depleting T cells. Though our current study does not address the downstream effect of these vascular changes as it relates to disease progression, it does highlight a possible role for endothelial cells in potentiating microglial reactivity through vascular function and peripheral immune cell interactions. Together these studies position endothelial cells as the gatekeepers to disease progression through the C3a-C3aR-VCAM1 axis.

In conclusion, our work identifies a novel complement regulatory axis at the BBB through endothelial C3aR. It implicates a critical role for a C3aR-dependent endothelial inflammatory transition which results in increased VCAM1 expression in the aged brain. Our data suggest that blocking complement-mediated effects can have a substantial impact in improving vascular health, rescuing BBB permeability, and decreasing neuroinflammation in aging and neurodegeneration. Since the complement pathway is upregulated in both acute inflammatory conditions, such as stroke and traumatic brain injury, and in neurodegenerative diseases, in particular AD of which age is the greatest risk factor, our findings have direct implications to the pathogenesis and therapeutic targeting of these age-related diseases of the brain.

Materials and Methods

Mice and treatment

The aged C57BL/6J mice were obtained from the NIH-NIA aging rodent colony. *C3ar1*-deficient mice (*C3ar1*$^{-/-}$) mice were obtained from the Jackson Laboratory and backcrossed to C57BL/6J for 5 generations. Mice were housed 2-4 per cage in a pathogen free mouse facility with ad libitum access to food and water on a 12 hr light/dark cycle. Mice for the conditional knockout studies were bred from a mixed background of Tie2^{cre} mice (C57BL/6J) and the *C3ar1*$^{fl/+}$ mice (BALB/c) (40). The breeding scheme for PS19 studies was previously published by Litvinchuk et al (22). Both males and females with approximately equal numbers were used for all experiments.

Vehicle (0.5% DMSO) or C3aR antagonist (C3aRA 1 mg/kg) were injected intraperitoneally (i.p.) every other day for 4 weeks. For intracerebroventricular (i.c.v.) administration of LPS, mice were placed in a Kopf stereotaxic instrument, and glass needles were inserted through bore holes using coordinates to target lateral ventricles (-0.4 mm anteroposterior, ± 1.0 mm mediolateral, and -2.0 mm dorsoventral from the surface of the skull at bregma). LPS (2 μg/ml) or vehicle (PBS) was administered bilaterally (2 μl each side).

BBB analysis was followed as previously described (35). Briefly, mice were injected via tail vein with 100 μls of 10 mg/ml stock TRITC–Dextran (MW 65-85 kDa; Sigma T1162). Dye was allowed to naturally perfuse for 2 hours and were then perfused with PBS. One hemisphere was used to determine TRITC fluorescence signal in tissue homogenates (excitation λ 550 nm, emission λ 580 nm) using a plate reader (Molecular Devices Spectra Max i3x). The other hemisphere was fixed in 4% PFA overnight at 4°C and switched to 30% sucrose. Sagittal brain sections (30 μm) were cut on a sliding microtome, washed in PBS, and stained with Lectin-649 (Vector Labs DL-1178) for 30 mins at RT in PBS containing 0.4% Triton X-100, 4% donkey serum, and 1% BSA to mark brain vasculature. The sections were imaged on a Leica TCS laser confocal microscope at 40x under oil immersion, with a z-step of 0.5 μm over a total range of 30 μm.

Cell culture

Primary HBMECs were obtained from Cell Systems (ACBRI 376). Cells were thawed and plated into T75 flasks for expansion in Lonza EGM2-MV medium (CC-3202) to reach a P4 culture. Cells were sub-cultured until confluent, passaged at a 1:4 ratio into T75 flasks for P5 cultures, and allowed to expand until confluent prior to freezing (EGM2-MV + 10% DMSO). Fresh vials were thawed to obtain P6 cultures which were used for all further experiments.

Primary human astrocytes were obtained from ScienCell Research Laboratories (AM 1800). Cells were thawed and plated into a T75 flask for expansion in ScienCell's Astrocyte Medium (AM 1801). Cells were sub-cultured until near confluence (80-90%), passaged at a 1:4 ratio into T75 flasks, and allowed to expand until near confluence prior to freezing (AM + 10% DMSO). Fresh vials were thawed and used for all further experiments.

Primary mouse astrocyte cultures were prepared as described previously *(20)* and purified using negative selection by magnetic CD11b beads (Miltenyi Biotec 130-049-601). Primary HBMECs were cultured on 100 µg/ml fibronectin and collagen IV coated 24 well or 48 well plates. Cells were seeded at a density of $2.5x10^5$ cells/cm^2. When confluent cells were treated with IL-1β (10 ng/ml, R&D 201-LB-005), C3a (500 nM, R&D 3677-C3-025), C5a (250 nM, R&D 2037-C5-025), Ionomycin (10 µM, Cayman 10004974), or in combination with one of the inhibitors SB290157 (5 µM, Calbiochem 559410), W7 (50 µM TOCRIS 0369) or BAPTA-AM (1 µM, TOCRIS 2787). Cells were analyzed after 2 hr or 24 hr treatment.

Trans-endothelial electrical resistance (TEER) analysis was performed using combinations of primary HBMECs and primary human or mouse astrocytes in a co-culture. Briefly, semi-permeable transwell inserts (Corning 3470) were coated with 100 µg/ml Fibronectin and Collagen IV on the luminal surface, for 2 hours at 37°C in PBS. The remaining coating solution was aspirated and the transwells were flipped over and placed into 12 well culture plates. The abluminal surface was coated with poly-D-lysine (PDL) at 37°C for 2 hr and the remaining solution was aspirated. While inverted, primary astrocytes were seeded to the abluminal surface at a

density of 1.5 x 10^5 cells/cm^2 and allowed to attach for 4-6 hrs at 37°C in 100µl AM from ScienCell. The membranes were then reverted to normal position in their original culture plate and the astrocytes were cultured in AM placed into the tissue culture plate (abluminal). The cells were cultured for 48 hours at 37°C and endothelial cells were seeded in the luminal compartment at a density of 1.5 x 10^5 cells/cm^2 in EGM2-MV. All TEER readings were measured using STX2 chopstick electrodes with an EVOM2 volt/ohm meter (World Precision Instruments). Cultures matured over 3-4 days, and when TEER stabilized (~160-180Ω) treatments were added and TEER was monitored over 24 hours. All TEER readings were normalized to the average reading from two cell free inserts for each time-point recording prior to normalization to the control samples.

Brain vessel preparations

Isolation of mouse brain vessels was carried out as previously described (28) with minor modifications. Briefly, mice were perfused with PBS, brains were removed, and cerebellum olfactory bulb and brain stem were discarded. They were stripped of dura and meninges, gently sliced with a razor blade, and gently homogenized using a glass Dounce homogenizer (Kontes Glass 19) all on ice. The homogenate was centrifuged, supernatant was discarded, and the pellet was resuspended in a dextran solution to remove myelin debris. The resulting pellet was then filtered over a 40 µm filter and vessel fragments were retained in the filter. The filter was then turned over, placed on a 50 ml conical tube, and rinsed. Vessel fragments were pelleted at 300xg for 5 minutes and fixed in 4% PFA for 30 minutes on ice. Fixed fragments were pelleted at 300xg for 5 minutes, washed with PBS, and mounted onto manually gridded slides for staining. Vessels were blocked with PBS containing 0.4% Triton X-100, 4% donkey serum, and 1% BSA for 30 min, and incubated in blocking solution with primary antibody overnight at 4°C. Depending on the experiment primary antibodies were used as follows: rabbit anti-GFAP (Millipore, G9269), rat anti-C3aR (Hycult, 10130173), and goat anti-mVE-cadherin (AF1002). Imaging was performed on a

Leica TCS laser confocal microscope at 63x under oil immersion, with a z-step of 0.5 µm over a total range of 10 µm.

Flow cytometry analysis

Flow cytometry analysis of aged brain lymphocytes was performed using CoBrA dissociation strategy as previously described (27) with slight modifications for myelin/debris removal, antibody staining, and for dissociation to sub-type lymphocyte markers. Briefly, adult mice were perfused with PBS, brain tissues were gently minced with sterile razor blades, digested in papain (Worthington Biochemical, LK003172) and DNase (Worthington Biochemical, LK003178), then triturated 3-4 times using a fire-polished glass Pasteur pipette. After incubation, papain digestion was neutralized with HBSS+ and the suspension was pelleted at 310 *g* for 5 minutes at 4°C. The pellet was resuspended in 1 ml of HBSS+, transferred to an ice-cold 1.7 ml Eppendorf tube and further triturated 3 times, and collecting the supernatant following a brief, low speed centrifugation. The supernatant at the end of each brief centrifugation was filtered through a prewetted 40 µm cell strainer (BD, 352340) into a chilled 50-ml conical tube and centrifuged at 310 *g* for 5 minutes at 4°C. The resulting pellet was depleted of myelin and other debris using a 20% isotonic Percoll PLUS (Millipore Sigma, E0414-250ML) separation. The resulting pellet contains dissociated single cells. For myeloid vs. lymphoid discrimination cells were incubated in 500 µl HBSS+ containing 1:100 Mouse BD Fc Block (BD Biosciences, 553141), 1:500 rat anti-CD45-BV421 (BD Biosciences, 563890), and 1:500 rat anti-CD11b-FITC (BD Biosciences, 553310) on ice for 15-20mins. For subtyping the lymphocyte populations, the tissue dissociation strategy was changed using Collagenase/Dispase (Millipore Sigma 10269638001) in place of papain to preserve the epitopes for CD19, CD8a, and CD4. All other steps of the dissociation strategy remained the same. Following tissue dissociation, cells were incubated in 1:500 rat anti-CD45-BUV395 (BD Biosciences, 564279), 1:500 rat anti-CD11b-FITC (BD, 553310), hamster anti-CD3ε-BV650 (BD, 564378), 1:500 rat anti-CD19-BV480 (BD, 566167), 1:500 rat anti-CD4-PE (BD, 553730), and

1:500 rat anti-CD8a-APC (BD, 553035) on ice for 15-20mins. Cells were washed twice with HBSS+ and resuspended in 500 µl of HBSS+ prior to flow cytometry analysis. Flow analysis was performed using a BD LSR Fortessa equipped with 355 nm, 405 nm, 488 nm, 561 nm, and 640 nm lasers to minimize spectral overlap.

For FACS of astrocytes and endothelial cells see the tissue preparation methods using papain. Following tissue dissociation cells were incubated in 500 µl HBSS+ containing 1:100 Mouse BD Fc Block (BD Biosciences, 553141) LIVE/DEAD Fixable Blue Dead Cell (Thermo Fisher, catalog L23105), 1:500 rat anti-CD45-BV421 (BD Biosciences, 563890), and 1:500 rat anti-CD11b-FITC (BD Biosciences, 553310), 1:250 anti-CD49a-VioBright PE (Miltenyi Biotec, 130-107-632); and 1:100 anti-ACSA-2-APC (Miltenyi Biotec, 130-116-245), on ice for 15 20 mins. Endothelial cells were sorted by first excluding $CD45^+$ and $CD11b^+$ cells, and gating around $CD49a^+$ cells. Astrocytes were sorted by gating triple-negativity for the former markers and finally gating around $ACSA2^+$ cells. Sorting was performed using a BD Aria II on the 100-micron nozzle. Cells were sorted into 1.7 ml Eppendorf tubes containing 200 µl HBSS+ followed by centrifugation and lysis of pellets in Qiagen RLT buffer containing 1% β-mercaptoethanol.

For flow cytometry of HBMECs, cells were singularized with Trypsin EDTA (Thermo Fisher 25200056) for 5 minutes and trypsin was neutralized using HBSS+. Cells were pelleted by centrifugation at 1500rpm and washed three times with HBSS+. Cells were fixed in 4% PFA for 20-30mins at 37˚ C. Following fixation, HBSS+ was added to tube prior to centrifugation to minimize cell loss. Cells were centrifuged at 1500rpm and washed three times with HBSS. Antibodies were diluted in HBSS+ and cells were stained with either appropriate IgG controls, or combination of rat anti-C3aR 1:500 (R&D MAB10417), mouse anti-Glut1 1:1000 (Thermo Fisher MA1-37783), and goat anti-VE-Cadherin 1:1000 (R&D MAB9381). Cells were incubated in antibody solution on a benchtop rotator for 30 minutes, then washed three times with HBSS+ and incubated in appropriate secondary antibodies for 30mins at room temperature in benchtop rotator. Cells were washed in HBSS+ three times prior to flow cytometry analysis.

Quantitative RT-PCR

RNA was extracted from cells using the RNeasy Micro kit (Qiagen, 74004). Reverse transcription was performed using the iScript Reverse Transcription Supermix (Bio-Rad, 1708840) according to the manufacturer's protocol. All RNA isolated from cell pellets was converted into cDNA. Quantitative RT-PCR was performed using iTaq Universal SYBR Green Supermix (Bio-Rad, 172-5120) on a CFX384 Touch Real-Time PCR Detection System.

Immunostaining and image analysis

Cultured cells were fixed with 4% PFA for 20 mins at 37°C. Samples were washed with PBS and then blocked and permeabilized with PBS containing 0.4% Triton X-100, 4% donkey serum, and 1% BSA for 30 min. Samples were incubated in blocking solution containing primary antibody overnight at 4°C. Depending on the experiment primary antibodies were used as follows: rabbit anti-pMLC2 S19 (Cell Signaling 3671), goat anti-hVE-cadherin (R&D AF938), or Phalloidin CruzFluor 555 (sc-363794). All images were taken on a Leica TCS laser confocal microscope at 40x or 63x under oil immersion, with a z-step of 0.5 µm over a total range of 5 µm. Mean fluorescence intensity was normalized to cell number per image and each condition consisted of 8-10 images (n=250-300 cells).

For mouse brain analysis, mice were perfused with 4% PFA, followed by 4% PFA post-fix overnight at 4°C and finally transferred into 30% sucrose solution until sectioning. Sagittal brain sections (30 mm) were cut on a sliding microtome and stored at -20°C in cryoprotectant. After washing in PBS, sections were blocked with PBS containing 0.4% Triton X-100, 4% donkey serum, and 1% BSA for 30 min, and then incubated in blocking solution containing primary antibody overnight at 4°C. Depending on the experiment primary antibodies were used as follows: rabbit anti-GFAP (Millipore, G9269), rat anti-C3 (Hycult, 10129042), rat anti-C3aR (Hycult, 10130173), anti-CD106 (Biolegend 305802) rat anti-CD31 (BD Biosciences 550274), goat anti-

mVE-cadherin (AF1002), goat anti-PDGFRβ (R&D AF 1042), mouse anti-Glut1 (Thermo Fisher MA1-37783) and rabbit anti-ColIV (Abcam ab6586). Following primary antibody staining sections were washed in 1x PBS three times and stained with appropriate secondary antibodies for 1-2 hours and washed again before mounting.

For quantification of VCAM1 in the mouse cortex and hippocampus, sections were stained with CD31 and VCAM1, then fluorescent signal was scanned using an EVOS FL Auto system at 10x. Images were then processed by ImageJ and background was subtracted before quantification. Total VCAM1 positive signal was quantified as percent area for each region, hippocampus or cortex. Colocalization of this signal with CD31 was confirmed for accuracy.

For quantification of percent occupancy of C3 in astrocytes Z-stacks (~30 µm thick with 0.5 µm step-size) were taken under 40x oil immersion, with labelling for C3, analyzed using the "Spots" feature of IMARIS 9.2.1 software. Spots were generated automatically for C3 representation. Subsequently, Z-stacks were analyzed using the "Co-loc" feature where $GFAP^+$ signal was used to mask astrocyte outlines, and thresholds applied to remove background. Data were then recorded as percent of ROI ($GFAP^+$ signal mask) occupied by the C3 (Spots) signal. Eight images spanning CA1-CA3 were taken across 5 mice per group.

For quantification of average vessel cross-sectional area Z-stacks (~30 µm thick with 0.5 µm step-size) were taken under 40x oil immersion, with labelling for ColIV. Images were first analyzed using the "Surfaces" feature of IMARIS 9.2.1 software to generate 3D reconstruction of the vessel and a total vessel volume in μm^3. Subsequently, using the "Filaments" function, the total vessel length per image was estimated by calculating individual vessel branch measurements in µm. Average cross-sectional area was determined by the proportional measurement of total vessel volume by total vessel length per image. Six images spanning CA1-CA3 were taken across 5 mice per group.

For quantification of tortuous vessel morphology Z-stacks (~30 µm thick with 0.5 µm step-size) were taken under 40x oil immersion, with labelling for CD31. Images were manually

quantified by counting the number of corkscrew vessels present in projected z-stack image. Images were projected in Leica LAS X software and manually scrolled through to count the number of corkscrew features in hippocampal vasculature. To represent this morphology representative images were taken under the same imaging parameters but under 63x oil immersion. The “Surfaces” function of IMARIS 9.2.1 software was used to generate 3D reconstruction of the CD31 vessel, and the animation tab was used to create movies. Six images spanning CA1-CA3 were taken across 5 mice per group for imaging quantification.

For quantification of microglial reactivity, CD68 colocalization in Iba1 signal was quantified using Z-stacks imaged on a Leica confocal microscope, with 40X oil objective, a 1.0 digital zoom, a total thickness of 25 µm, and with 1 µm step-size. Percent colocalization of CD68 signal within the masked Iba1 ROI was calculated using the “Co-loc” feature in IMARIS and represented as a fold change of this percentage.

To quantify the volume of hippocampus and entorhinal cortex mouse frozen brain tissues were serially cut at 50 μm. Sections containing hippocampus or entorhinal cortex (every sixth section, 300 μm apart) between bregma +2.1mm and bregma −3.9 mm to the dorsal end of the hippocampus or entorhinal cortex were stained with 0.25% cresyl violet solution, dehydrated in ethanol and then mounted. Slides were imaged using Nanozoomer 2.0-HT system (Hamamatsu), and areas of interest were traced using NDP Viewer software. The volume of the region of interest was quantified using the following formula: volume = (sum of area) * 0.5 mm.

RNA-sequencing analysis

RNA sequencing data containing fold changes and adjusted p values from our previous study (22) was used (GEO: GSE114910). For pathway analyses, differentially expressed genes with p (adj) values of <0.05 were uploaded into the InnateDB website, and overrepresentation analysis was used to calculate significant terms from KEGG and REACTOME databases. Selected

significant terms were plotted by p value based on their involvement in vascular biology and immune cell infiltration, and representative genes contributing to the hits were listed. For individual gene plots, FPKM values were used and significance was calculated using one-way ANOVA.

Statistical Analysis

All statistical analysis was performed using GraphPad Prism software v8.0.2. All data are presented as mean ± SEM. Unless otherwise noted, all grouped comparisons were made by one-way ANOVA with Tukey's correction, and all pairwise comparisons by two-sided Student's t-tests, depending on experimental design. For all tests P values less than 0.05 were considered significant, and those over 0.05 were considered non-significant.

Study Approvals

All animal procedures were performed in accordance with NIH guidelines and with the approval of the Baylor College of Medicine Institutional Animal Care and Use Committee.

Author Contributions

NEP and HZ conceived of the project and designed the experiments. NEP performed all experiments and data analysis unless otherwise noted. ER provided reagents, technical assistance for IMARIS imaging analysis, performed pathway analysis, and edited the manuscript. AL provided samples, technical assistance, and performed brain volumetric tissue analysis. JK provided the *C3ar1* floxed mice. NEP wrote the manuscript with input and revision from HZ. All authors read and approved the final manuscript.

Acknowledgements

We are indebted to D. Holtzman (Wash U. St Louis) for the generous support with the brain volumetric analysis. We are most appreciative to NIA for offering aged C57BL6/J mice that made this work possible. We thank C. Beeton, J. Sederstrom and the Baylor College of Medicine Cytometry and Cell Sorting Core supported by grant NCI-CA125123 for FACS analysis. We are grateful to N. Aithmitti and B. Contreras for expert technical support and members of the Zheng laboratory for stimulating discussions. This study was supported by grants from the NIH (R01 NS093652, R01 AG020670, R01 AG057509, RF1 AG054111 and RF1 AG062257 to HZ).

References

1. Lindenberger U. Human Cognitive Aging: *Corriger la fortune? Science* 2014;346(6209):572-8.
2. Maniega SM, Valdes Hernandez MC, Clayden JD, Royle NA, Murray C, Morris Z, et al. White matter hyperintensities and normal-appearing white matter integrity in the aging brain. *Neurobiol Aging.* 2015;36(2):909-18.
3. Kalamakis G, Brüne D, Ravichandran S, Bolz J, Fan W, Ziebell F, et al. Quiescence Modulates Stem Cell Maintenance and Regenerative Capacity in the Aging Brain. *Cell.* 2019;176(6):1407-19.e14.
4. Miranda CJ, Braun L, Jiang Y, Hester ME, Zhang L, Riolo M, et al. Aging brain microenvironment decreases hippocampal neurogenesis through Wnt-mediated survivin signaling. *Aging Cell.* 2012;11(3):542-52.
5. Sweeney MD, Kisler K, Montagne A, Toga AW, and Zlokovic BV. The role of brain vasculature in neurodegenerative disorders. *Nat Neurosci.* 2018;21(10):1318-31.
6. Sun D, McGinn M, Hankins JE, Mays KM, Rolfe A, and Colello RJ. Aging- and injury-related differential apoptotic response in the dentate gyrus of the hippocampus in rats following brain trauma. *Front Aging Neurosci.* 2013;5:95.
7. Dhungana H, Malm T, Denes A, Valonen P, Wojciechowski S, Magga J, et al. Aging aggravates ischemic stroke-induced brain damage in mice with chronic peripheral infection. *Aging Cell.* 2013;12(5):842-50.
8. Sweeney MD, Sagare AP, and Zlokovic BV. Blood-brain barrier breakdown in Alzheimer disease and other neurodegenerative disorders. *Nat Rev Neurol.* 2018;14(3):133-50.
9. Marchant NL, Reed BR, Sanossian N, Madison CM, Kriger S, Dhada R, et al. The aging brain and cognition: contribution of vascular injury and abeta to mild cognitive dysfunction. *JAMA Neurol.* 2013;70(4):488-95.
10. Montagne A, Nation DA, Sagare AP, Barisano G, Sweeney MD, Chakhoyan A, et al. APOE4 leads to blood-brain barrier dysfunction predicting cognitive decline. *Nature.* 2020;581(7806):71-6.
11. Yousef H, Czupalla CJ, Lee D, Chen MB, Burke AN, Zera KA, et al. Aged blood impairs hippocampal neural precursor activity and activates microglia via brain endothelial cell VCAM1. *Nat Med.* 2019;25(6):988-1000.
12. Perner C, Perner F, Gaur N, Zimmermann S, Witte OW, Heidel FH, et al. Plasma VCAM1 levels correlate with disease severity in Parkinson's disease. *J Neuroinflammation.* 2019;16(1):94.
13. Dulken BW, Buckley MT, Navarro Negredo P, Saligrama N, Cayrol R, Leeman DS, et al. Single-cell analysis reveals T cell infiltration in old neurogenic niches. *Nature.* 2019;571(7764):205-10.
14. Gate D, Saligrama N, Leventhal O, Yang AC, Unger MS, Middeldorp J, et al. Clonally expanded CD8 T cells patrol the cerebrospinal fluid in Alzheimer's disease. *Nature.* 2020;577(7790):399-404.
15. Chen MB, Yang AC, Yousef H, Lee D, Chen W, Schaum N, et al. Brain Endothelial Cells Are Exquisite Sensors of Age-Related Circulatory Cues. *Cell Rep.* 2020;30(13):4418-32 e4.
16. Katsimpardi L, Litterman NK, Schein PA, Miller CM, Loffredo FS, Wojtkiewicz GR, et al. Vascular and neurogenic rejuvenation of the aging mouse brain by young systemic factors. *Science.* 2014;344(6184):630-4.
17. Baker DJ, and Petersen RC. Cellular senescence in brain aging and neurodegenerative diseases: evidence and perspectives. *J Clin Invest.* 2018;128(4):1208-16.
18. Stephan AH, Barres BA, and Stevens B. The complement system: an unexpected role in synaptic pruning during development and disease. *Annu Rev Neurosci.* 2012;35:369-89.

19. Shi Q, Chowdhury S, Ma R, Le KX, Hong S, Caldarone BJ, et al. Complement C3 deficiency protects against neurodegeneration in aged plaque-rich APP/PS1 mice. *Sci Transl Med.* 2017;9(392).
20. Shi Q, Colodner KJ, Matousek SB, Merry K, Hong S, Kenison JE, et al. Complement C3-Deficient Mice Fail to Display Age-Related Hippocampal Decline. *J Neurosci.* 2015;35(38):13029-42.
21. Lian H, Yang L, Cole A, Sun L, Chiang AC, Fowler SW, et al. NFkappaB-activated astroglial release of complement C3 compromises neuronal morphology and function associated with Alzheimer's disease. *Neuron.* 2015;85(1):101-15.
22. Litvinchuk A, Wan YW, Swartzlander DB, Chen F, Cole A, Propson NE, et al. Complement C3aR Inactivation Attenuates Tau Pathology and Reverses an Immune Network Deregulated in Tauopathy Models and Alzheimer's Disease. *Neuron.* 2018;100(6):1337-53 e5.
23. Hong S, Beja-Glasser VF, Nfonoyim BM, Frouin A, Li S, Ramakrishnan S, et al. Complement and microglia mediate early synapse loss in Alzheimer mouse models. *Science.* 2016;352(6286):712-6.
24. Boire A, Zou Y, Shieh J, Macalinao DG, Pentsova E, and Massague J. Complement Component 3 Adapts the Cerebrospinal Fluid for Leptomeningeal Metastasis. *Cell.* 2017;168(6):1101-13 e13.
25. Schraufstatter IU, Trieu K, Sikora L, Sriramarao P, and DiScipio R. Complement c3a and c5a induce different signal transduction cascades in endothelial cells. *J Immunol.* 2002;169(4):2102-10.
26. Boisvert MM, Erikson GA, Shokhirev MN, and Allen NJ. The Aging Astrocyte Transcriptome from Multiple Regions of the Mouse Brain. *Cell Rep.* 2018;22(1):269-85.
27. Swartzlander DB, Propson NE, Roy ER, Saito T, Saido T, Wang B, et al. Concurrent cell type–specific isolation and profiling of mouse brains in inflammation and Alzheimer's disease. *JCI Insight.* 2018;3(13).
28. Boulay A-C, Saubaméa B, Declèves X, and Cohen-Salmon M. Purification of Mouse Brain Vessels. *J Vis Exp.* 2015;105(105).
29. Wu F, Zou Q, Ding X, Shi D, Zhu X, Hu W, et al. Complement component C3a plays a critical role in endothelial activation and leukocyte recruitment into the brain. *J Neuroinflammation.* 2016;13:23.
30. Van Beek J, Bernaudin M, Petit E, Gasque P, Nouvelot A, MacKenzie ET, et al. Expression of receptors for complement anaphylatoxins C3a and C5a following permanent focal cerebral ischemia in the mouse. *Exp Neurol.* 2000;161(1):373-82.
31. Ritzel RM, Crapser J, Patel AR, Verma R, Grenier JM, Chauhan A, et al. Age-Associated Resident Memory CD8 T Cells in the Central Nervous System Are Primed To Potentiate Inflammation after Ischemic Brain Injury. *J Immunol.* 2016;196(8):3318-30.
32. Pi J, Cheng Y, Sun H, Chen X, Zhuang T, Liu J, et al. Apln-CreERT:mT/mG reporter mice as a tool for sprouting angiogenesis study. *BMC Ophthalmol.* 2017;17(1):163.
33. Thore CR, Anstrom JA, Moody DM, Challa VR, Marion MC, and Brown WR. Morphometric Analysis of Arteriolar Tortuosity in Human Cerebral White Matter of Preterm, Young, and Aged Subjects. *Journal of Neuropathology and Experimental Neurology.* 2007;66(5):337-45.
34. Bullitt E, Zeng D, Gerig G, Aylward S, Joshi S, Smith JK, et al. Vessel Tortuosity and Brain Tumor Malignancy. *Academic Radiology.* 2005;12(10):1232-40.
35. Hu J, Dziumbla S, Lin J, Bibli S-I, Zukunft S, De Mos J, et al. Inhibition of soluble epoxide hydrolase prevents diabetic retinopathy. *Nature.* 2017;552(7684):248-52.
36. Shaftel SS, Carlson TJ, Olschowka JA, Kyrkanides S, Matousek SB, and O'Banion MK. Chronic interleukin-1beta expression in mouse brain leads to leukocyte infiltration and neutrophil-independent blood brain barrier permeability without overt neurodegeneration. *J Neurosci.* 2007;27(35):9301-9.

37. Wu MC, Brennan FH, Lynch JP, Mantovani S, Phipps S, Wetsel RA, et al. The receptor for complement component C3a mediates protection from intestinal ischemia-reperfusion injuries by inhibiting neutrophil mobilization. *Proc Natl Acad Sci U S A.* 2013;110(23):9439-44.
38. Shi Y, Zhang L, Pu H, Mao L, Hu X, Jiang X, et al. Rapid endothelial cytoskeletal reorganization enables early blood–brain barrier disruption and long-term ischaemic reperfusion brain injury. *Nature Communications.* 2016;7(1):10523.
39. Tietz S, and Engelhardt B. Brain barriers: Crosstalk between complex tight junctions and adherens junctions. *J Cell Biol.* 2015;209(4):493-506.
40. Quell KM, Karsten CM, Kordowski A, Almeida LN, Briukhovetska D, Wiese AV, et al. Monitoring C3aR Expression Using a Floxed tdTomato-C3aR Reporter Knock-in Mouse. *J Immunol.* 2017;199(2):688-706.
41. Kisanuki YY, Hammer RE, Miyazaki J, Williams SC, Richardson JA, and Yanagisawa M. Tie2-Cre transgenic mice: a new model for endothelial cell-lineage analysis in vivo. *Dev Biol.* 2001;230(2):230-42.
42. Tanaka Y, Adams DH, Hubscher S, Hirano H, Siebenlist U, and Shaw S. T-cell adhesion induced by proteoglycan-immobilized cytokine MIP-lβ. *Nature.* 1993;361(6407):79-82.
43. Kolev M, West EE, Kunz N, Chauss D, Moseman EA, Rahman J, et al. Diapedesis-Induced Integrin Signaling via LFA-1 Facilitates Tissue Immunity by Inducing Intrinsic Complement C3 Expression in Immune Cells. *Immunity.* 2020;52(3):513-27 e8.
44. Nation DA, Sweeney MD, Montagne A, Sagare AP, D'Orazio LM, Pachicano M, et al. Blood-brain barrier breakdown is an early biomarker of human cognitive dysfunction. *Nat Med.* 2019;25(2):270-6.
45. Montagne A, Barnes SR, Sweeney MD, Halliday MR, Sagare AP, Zhao Z, et al. Blood-brain barrier breakdown in the aging human hippocampus. *Neuron.* 2015;85(2):296-302.
46. Iadecola C. Dangerous leaks: blood-brain barrier woes in the aging hippocampus. *Neuron.* 2015;85(2):231-3.
47. Banks WA, Gray AM, Erickson MA, Salameh TS, Damodarasamy M, Sheibani N, et al. Lipopolysaccharide-induced blood-brain barrier disruption: roles of cyclooxygenase, oxidative stress, neuroinflammation, and elements of the neurovascular unit. *J Neuroinflammation.* 2015;12:223.
48. Yang AC, Stevens MY, Chen MB, Lee DP, Stahli D, Gate D, et al. Physiological blood-brain transport is impaired with age by a shift in transcytosis. *Nature.* 2020;583(7816):425-30.
49. Marsh SE, Abud EM, Lakatos A, Karimzadeh A, Yeung ST, Davtyan H, et al. The adaptive immune system restrains Alzheimer's disease pathogenesis by modulating microglial function. *Proc Natl Acad Sci U S A.* 2016;113(9):E1316-25.
50. Laurent C, Dorothee G, Hunot S, Martin E, Monnet Y, Duchamp M, et al. Hippocampal T cell infiltration promotes neuroinflammation and cognitive decline in a mouse model of tauopathy. *Brain.* 2017;140(1):184-200.
51. Faraco G, Hochrainer K, Segarra SG, Schaeffer S, Santisteban MM, Menon A, et al. Dietary salt promotes cognitive impairment through tau phosphorylation. *Nature.* 2019;574(7780):686-90.

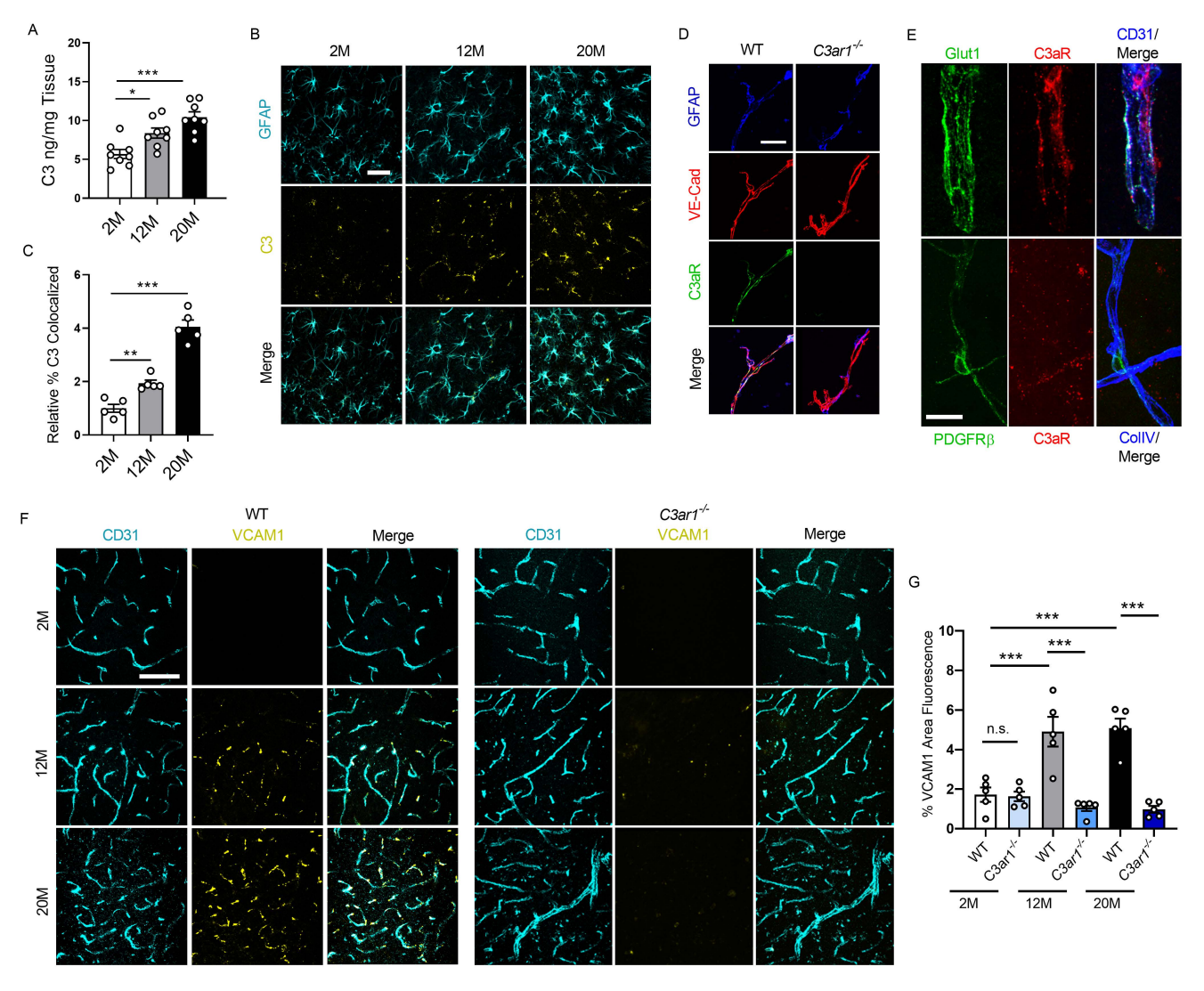
A
C3 ng/mg Tissue
20
15
10
5
0
***
*
2M
12M
20M
B
2M
12M
20M
GFAP
C3
Merge
C
Relative % C3 Colocalized
6
4
2
0
***
**
2M
12M
20M
D
WT
C3ar1-/-
GFAP
VE-Cad
C3aR
Merge
E
Glut1
C3aR
CD31/
Merge
PDGFRβ
C3aR
ColIV/
Merge
F
WT
C3ar1-/-
CD31
VCAM1
Merge
CD31
VCAM1
Merge
2M
12M
20M
G
% VCAM1 Area Fluorescence
10
8
6
4
2
0
***
***
***
n.s.
WT
C3ar1-/-
WT
C3ar1-/-
WT
C3ar1-/-
2M
12M
20M

Figure 1. C3a-C3aR signaling regulates age-associated endothelial VCAM1 expression. (A) ELISA measurement of C3 levels in wild-type mouse brain lysates at 2, 12 and 20 months (n=8/group). **(B)** Immunofluorescence staining using anti-GFAP and anti-C3 antibodies demonstrates localization of C3 to astrocytes. **(C)** Quantification confirming increased C3 staining within $GFAP^{+}$ astrocytes in the hippocampus with age (n=5/age). **(D)** Triple immunostaining of isolated vessels from wild-type (WT) and *C3ar1*$^{-/-}$ brains using anti-GFAP, anti-VE-Cadherin and anti-C3aR antibodies showing positive C3aR staining along endothelial cell surface which is not present in *C3ar1*$^{-/-}$ vessels. **(E)** Triple immunostaining of brain tissue with anti-Glut1, and anti-CD31 or anti-PDGFRβ, anti-C3aR, anti-Col IV demonstrating expression of C3aR on brain endothelial cells but not pericytes. **(F, G)** Immunofluorescence staining and quantification using anti-CD31 and anti-VCAM1 antibodies, of WT or *C3ar1*$^{-/-}$ mouse cortices at 2, 12, and 20 months demonstrates an increase in VCAM1 with age in WT mice but rescued in the absence of C3aR. All data are means ± SEM. Significance was calculated using one-way ANOVA with Tukey's post hoc test (*p <.05, **p<.01, ***p<.001). n.s.: not significant. Scale bar (B) = 20 µm, (D) = 10 µm, (E) = 15 µm, and (F) = 50 µm.

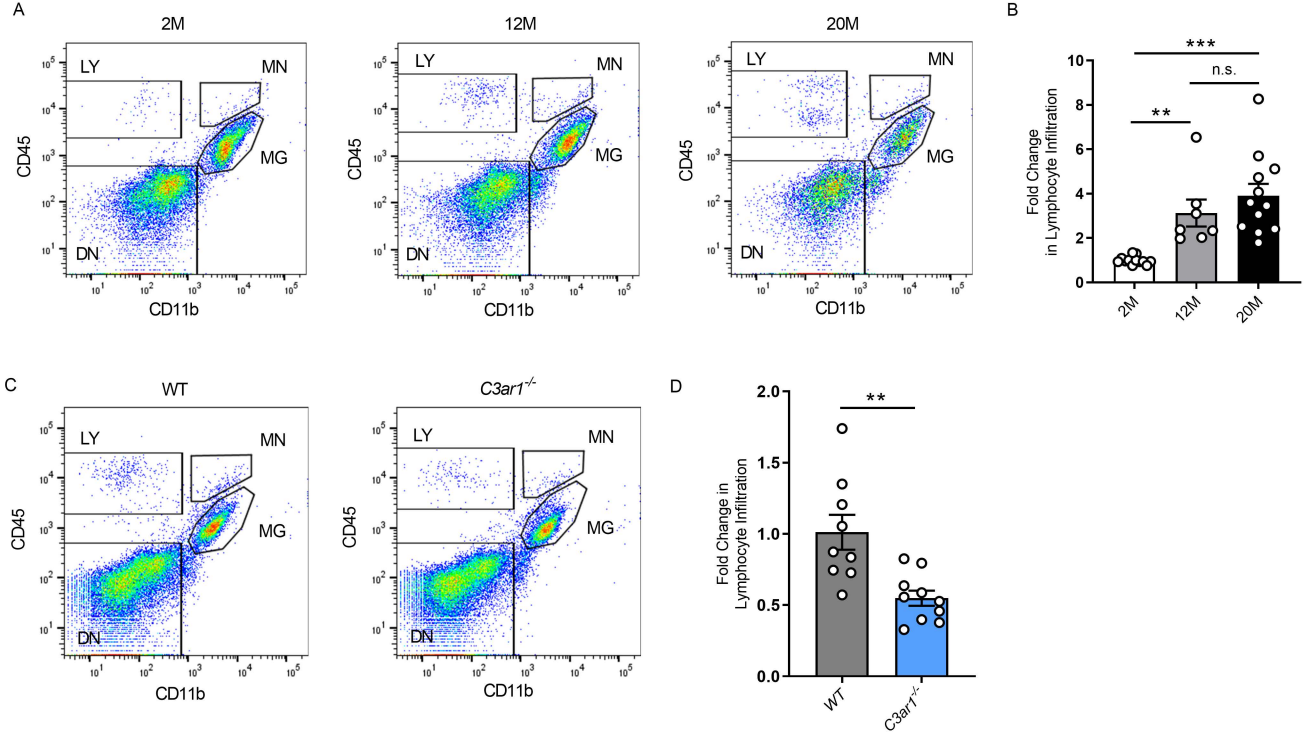
A
2M
12M
20M
LY
MN
MG
DN
CD45
CD11b
B
Fold Change in Lymphocyte Infiltration
***
n.s.
**
2M
12M
20M
C
WT
C3ar1-/-
D
Fold Change in Lymphocyte Infiltration
**
WT
C3ar1-/-

Figure 2. C3aR-VCAM1 axis promotes peripheral lymphocyte infiltration during aging. (A) Representative CD45 and CD11b flow cytometry plots and gating strategy of dissociated mouse brain at 2M, 12M and 20M; LY: lymphocyte; MN: monocyte; MG: microglia; DN: double-negative. **(B)** Flow cytometry analysis and quantification of percentage of infiltrating lymphocytes (2M n=12, 12M n=7, 20M n=12) shows age-related increase. **(C and D)** Flow cytometry analysis and quantification of brain lymphocytes in 12-14-month-old wild-type (WT, n=9) and *C3ar1*$^{-/-}$ (n=10) mice shows reduction in aged *C3ar1*$^{-/-}$ mice. All data are means ± SEM. Significance was calculated using one-way ANOVA with Tukey's post hoc test (**p<.01, ***p<.001). n.s.: not significant.

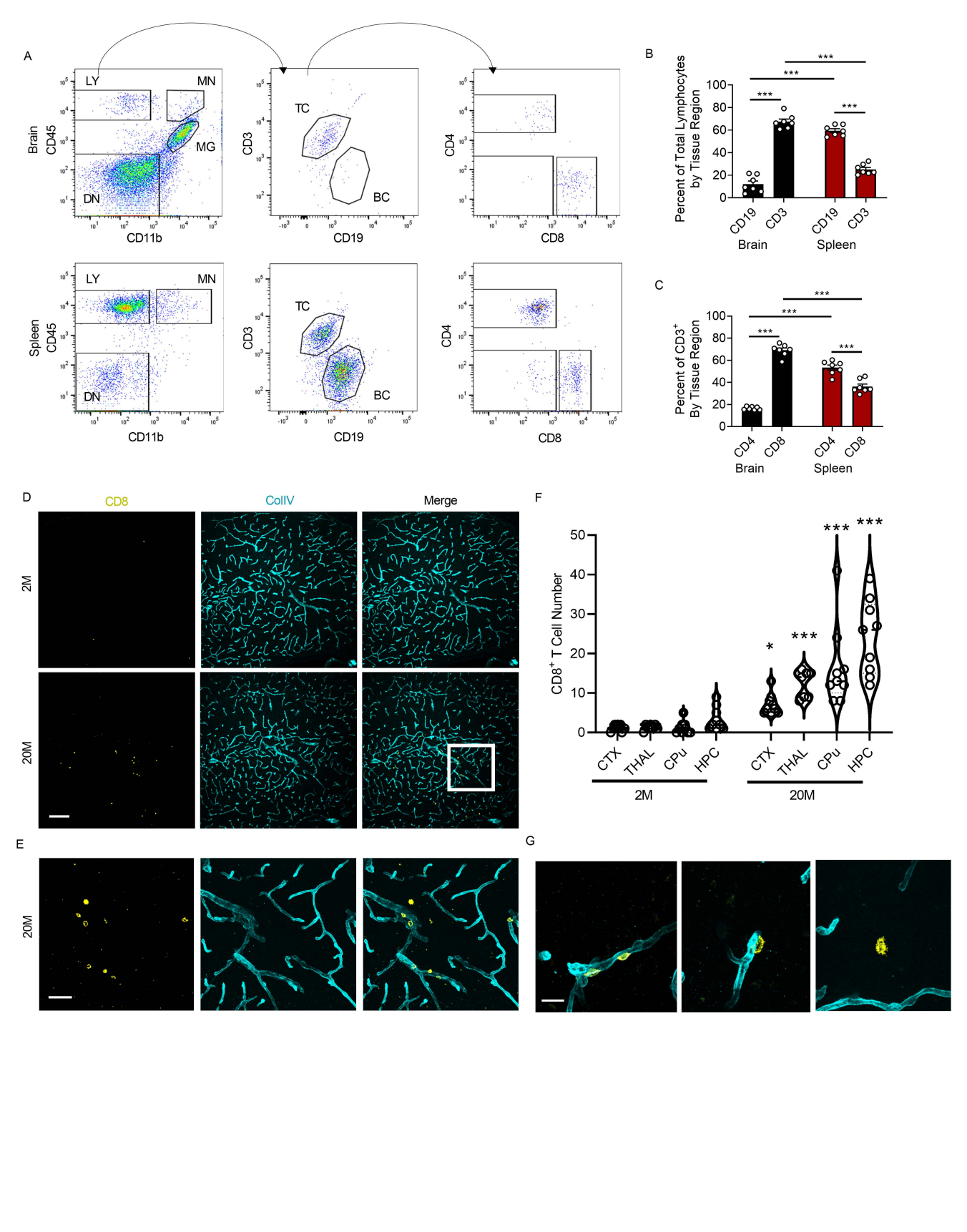
A
Brain
CD45
CD11b
LY
MN
MG
DN
CD3
CD19
TC
BC
CD4
CD8
Spleen
B
Percent of Total Lymphocytes by Tissue Region
CD19
CD3
Brain
Spleen
C
Percent of CD3+ By Tissue Region
CD4
CD8
D
CD8
ColIV
Merge
2M
20M
E
F
CD8+ T Cell Number
CTX
THAL
CPu
HPC
G

Figure 3. CD8$^+$ T cells are preferentially recruited and infiltrate the aged brain. **(A)** Schematic for flow cytometry analysis of dissociated infiltrating cells in the 20M brain or spleen using antibody staining against CD45, CD11b, CD3ε, CD19, CD8a, and CD4. LY: lymphocyte; MN: monocyte; MG: microglia; DN: double-negative; TC: T cells; BC: B cells. **(B)** Quantification of flow cytometry analysis shows predominantly CD3$^+$ T cells in the brain compared to the spleen which shows predominantly CD19$^+$ B cells (n=7/group). **(C)** Quantification of T cells shows the predominant sub-type enriched in the brain is CD8$^+$ T cells compared to CD4$^+$ T cells in the spleen (n=7/group). **(D)** Representative immunostaining of 2M and 20M brain tissue using anti-CD8a and anti-Col IV to determine regional immune cell infiltration within the brain. **(E)** Magnified image from (D) highlighting the infiltrated cell types which were counted for analysis. **(F)** Quantification of regional distribution of CD8$^+$ T cell infiltrates in four major brain regions (n=4/group, 2 tissue sections per mouse). CTX: cortex; THAL: thalamus; CPu: caudate putamen (CPu); HPC: hippocampus. **(G)** Representative images of three distinct stages of infiltration observed in all brain regions: perivascular residence (left panel), extravasation (middle panel), and parenchymal surveillance (right panel). Data in (B) and (C) are means ± SEM. Analysis was done using One-way ANOVA with Tukey's post hoc test (***p<.001). Data in (F) are violin plots displaying medians and quartile ranges. Analysis was done using Two-way ANOVA with Holm-Sidak's post hoc test (*p <.05, ***p<.001). Scale Bar (D) = 100 µm, (E) = 50 µm, (G) = 10 µm.

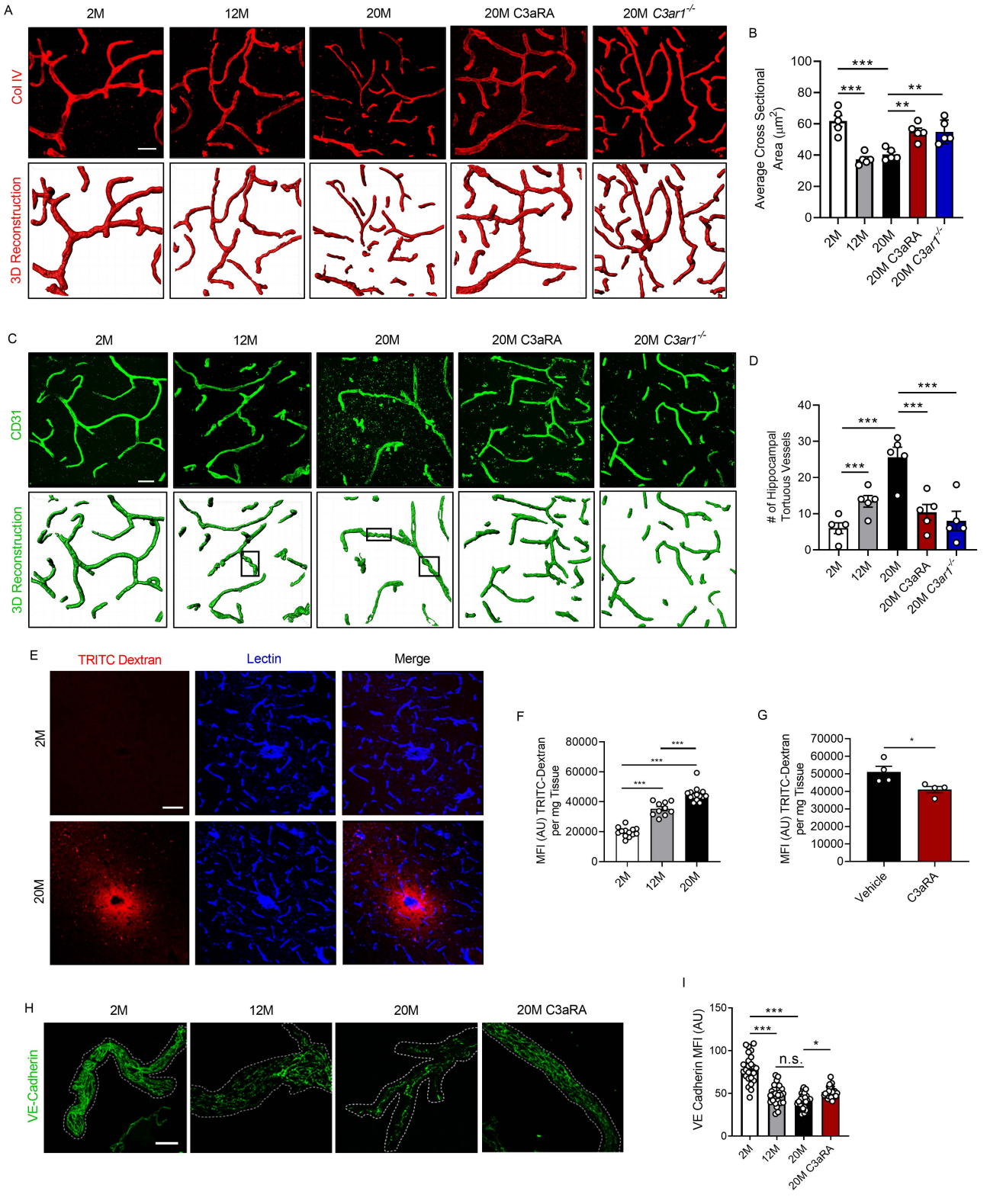
A
2M
12M
20M
20M C3aRA
20M C3ar1-/-
Col IV
3D Reconstruction
B
Average Cross Sectional Area (μm2)
2M
12M
20M
20M C3aRA
20M C3ar1-/-
C
CD31
3D Reconstruction
D
# of Hippocampal Tortuous Vessels
E
TRITC Dextran
Lectin
Merge
F
MFI (AU) TRITC-Dextran per mg Tissue
G
Vehicle
C3aRA
H
VE-Cadherin
I
VE Cadherin MFI (AU)
n.s.

Figure 4. Inhibition of C3aR rescues age-related changes in vascular morphology and BBB permeability. (A) Representative Collagen IV^{+} (Col IV) staining and IMARIS-aided 3D reconstruction of vasculature in hippocampal sections from 2M, 12M and 20M WT mice, 20M WT mice treated with C3aRA, or 20M *C3ar1*$^{-/-}$ mice. **(B)** Quantification of capillary average cross-sectional area in (A) (n=5/group, 8 images per mouse). **(C)** Representative CD31^{+} staining and 3D reconstruction of hippocampal vasculature in 2M, 12M and 20M WT mice, 20M WT mice treated with C3aRA or 20M *C3ar1*$^{-/-}$ mice. Representative tortuous vessels are marked by rectangles. **(D)** Quantification of number of tortuous vessels per hippocampal areas (n=5/group, 8 images per mouse). **(E)** Representative lectin and TRITC-Dextran co-labeling in 2M and 20M hippocampi. **(F)** Quantification of TRITC-Dextran mean fluorescence intensity (MFI) from brain lysates of 2M (n=13), 12M (n=10) and 20M (n=14) mice. **(G)** Quantification of TRITC-Dextran MFI of 20-month-old mice treated with vehicle or C3aRA (n=4/group). **(H)** Representative image of vessels isolated from 2M and 12M mice or 20M mice treated with vehicle or C3aRA and stained with anti-VE-Cadherin. **(I)** Quantification of VE-Cadherin staining shows reduced VE-Cadherin expression in 12M and 20M mice, which is partially rescued in 20M mice treated with C3aRA (n=5/group, 5 vessel fragments/mouse). All data are means ± SEM. Significance was calculated using one-way ANOVA with Tukey's post hoc test (*p <.05, **p<.01, ***p<.001). n.s.: not significant. Scale bar (A) and (C) = 20 µm; (E) = 50 µm.

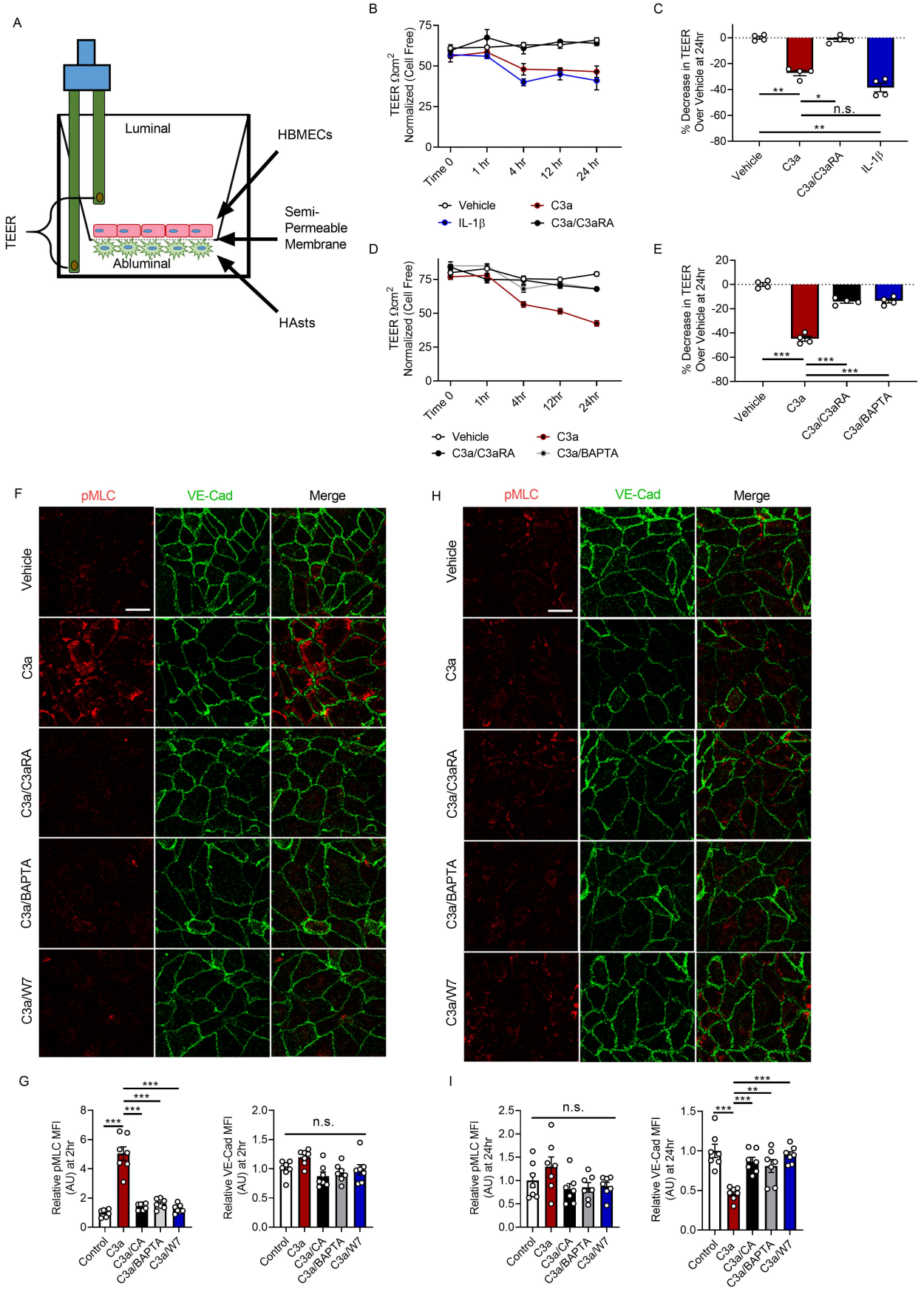
A
Luminal
HBMECs
TEER
Semi-
Permeable
Membrane
Abluminal
HAsts
B
TEER Ωcm2
Normalized (Cell Free)
Time 0
1 hr
4 hr
12 hr
24 hr
Vehicle
C3a
IL-1β
C3a/C3aRA
C
% Decrease in TEER
Over Vehicle at 24hr
n.s.
Vehicle
C3a
C3a/C3aRA
IL-1β
D
TEER Ωcm2
Normalized (Cell Free)
Time 0
1hr
4hr
12hr
24hr
Vehicle
C3a
C3a/C3aRA
C3a/BAPTA
E
% Decrease in TEER
Over Vehicle at 24hr
Vehicle
C3a
C3a/C3aRA
C3a/BAPTA
F
pMLC
VE-Cad
Merge
Vehicle
C3a
C3a/C3aRA
C3a/BAPTA
C3a/W7
H
pMLC
VE-Cad
Merge
Vehicle
C3a
C3a/C3aRA
C3a/BAPTA
C3a/W7
G
Relative pMLC MFI
(AU) at 2hr
Relative VE-Cad MFI
(AU) at 2hr
n.s.
Control
C3a
C3a/CA
C3a/BAPTA
C3a/W7
I
Relative pMLC MFI
(AU) at 24hr
Relative VE-Cad MFI
(AU) at 24hr
n.s.
Control
C3a
C3a/CA
C3a/BAPTA
C3a/W7

Figure 5. C3a-mediated barrier disruption is dependent on Ca^{2+} mobilization and alters VE-Cadherin through cytoskeletal activation. (A) Schematic of TEER analysis using a co-culture of astrocytes and endothelial cells. **(B)** TEER values in co-cultures treated with vehicle, C3a, C3a with C3aRA, or IL-1β for 0, 1, 4, 12 and 24 hrs. **(C)** Quantification of percent reduction of TEER at 24 hrs from treatments recorded in (B). **(D)** TEER values in co-cultures treated with vehicle, C3a or C3a with C3aRA or BAPTA-AM over 24 hrs. **(E)** Quantification of percent reduction in TEER at 24 hrs from treatments recorded in (D). All TEER experiments were performed two times with duplicates each and normalized to time-point control wells of cell free membranes. **(F)** Representative immunofluorescence images of human brain microvascular endothelial cells (HBMECs) treated with vehicle, C3a, or a combination of C3a plus C3aRA (C3a/C3aRA), BAPTA-AM (C3a/BAPTA), or W7 (C3a/W7) for 2 hrs and stained with anti-pMLC and anti-VE-Cadherin antibodies. **(G)** Quantification of pMLC or VE-Cadherin MFI shows increase in pMLC, but not VE-cadherin, (n=7 areas from three replicates of 250-300 cells/condition). **(H)** Representative immunofluorescence images of HBMECs treated as stated in (F) using anti-pMLC and anti-VE-Cadherin antibodies 24 hrs post-treatment. **(K)** Quantification of pMLC or VE-Cadherin MFI shows normalized pMLC levels but decreased VE-Cadherin (n=7 areas from three replicates of 250-300 cells/condition). All data are means ± SEM. Analysis was performed on average percent decrease in TEER using one-way ANOVA with Tukey's post hoc test (*p <.05, **p<.01, ***p<.001). n.s.: not significant. Scale bar = 10 μm.

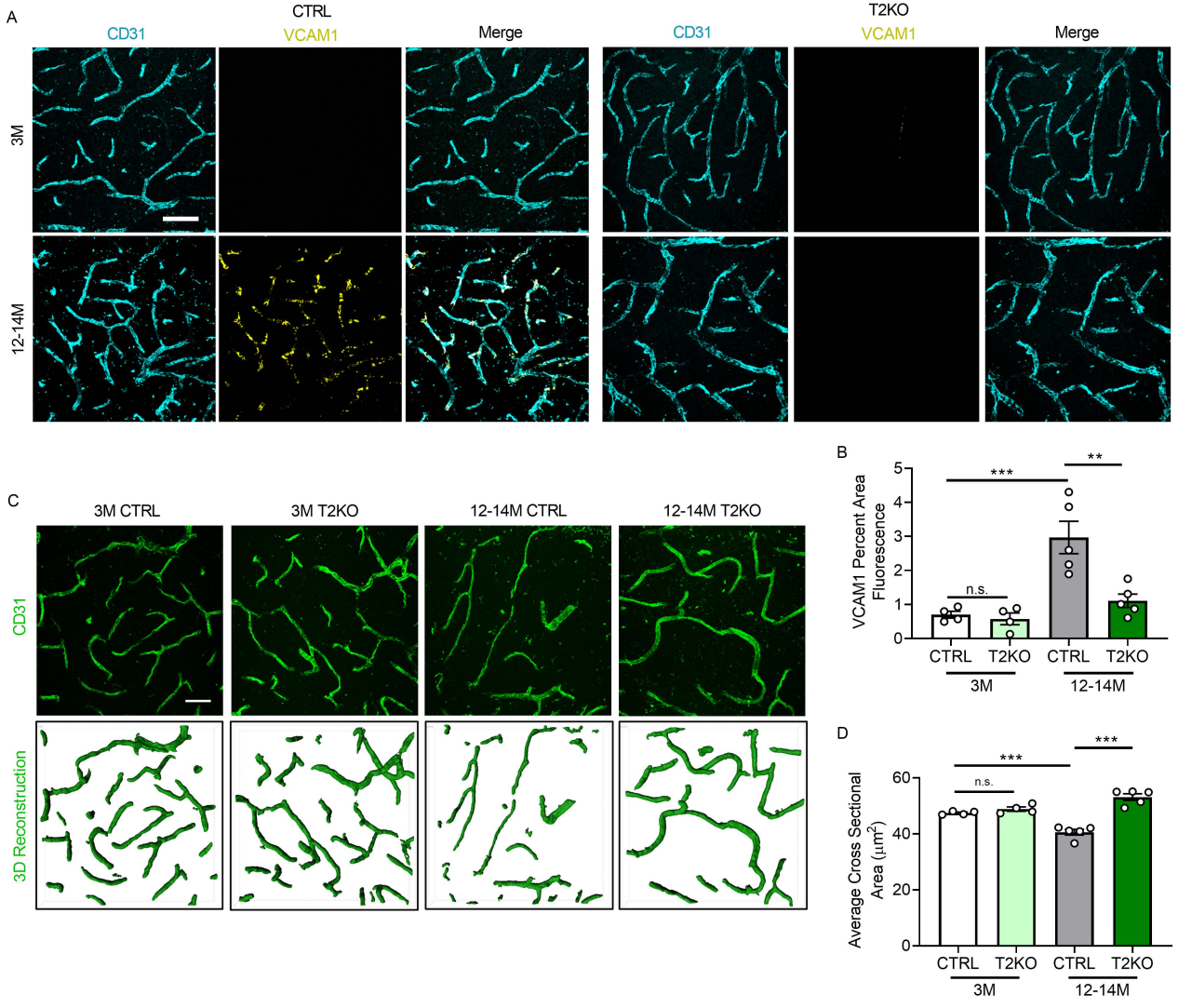
A
CTRL
T2KO
CD31
VCAM1
Merge
CD31
VCAM1
Merge
3M
12-14M
B
VCAM1 Percent Area Fluorescence
***
**
n.s.
CTRL
T2KO
CTRL
T2KO
3M
12-14M
C
3M CTRL
3M T2KO
12-14M CTRL
12-14M T2KO
CD31
3D Reconstruction
D
Average Cross Sectional Area (μm²)
***
***
n.s.
CTRL
T2KO
CTRL
T2KO
3M
12-14M

Figure 6. Conditional knockout of *C3ar1* in brain endothelial cells rescues age-related vascular phenotypes. **(A)** Representative VCAM1 and CD31 double staining images from 3M and 12-14M endothelial *C3ar1* conditional knockout (T2KO) mice and littermate controls (CTRL) showing increased in VCAM1 expression with age in CTRL mice but suppressed in T2KO. **(B)** Quantification of VCAM1 intensity of (A). **(C)** Representative CD31 staining and 3D reconstruction of 3M and 12-14M CTRL and T2KO mice. **(D)** Quantification of average $CD31^+$ cross sectional areas. All data are means ± SEM of n=4/group. Analysis for (A-F) was performed using one-way ANOVA with Tukey's post hoc test (**p<.01, ***p<.001). n.s.: not significant. Scale bar = 50 µm.

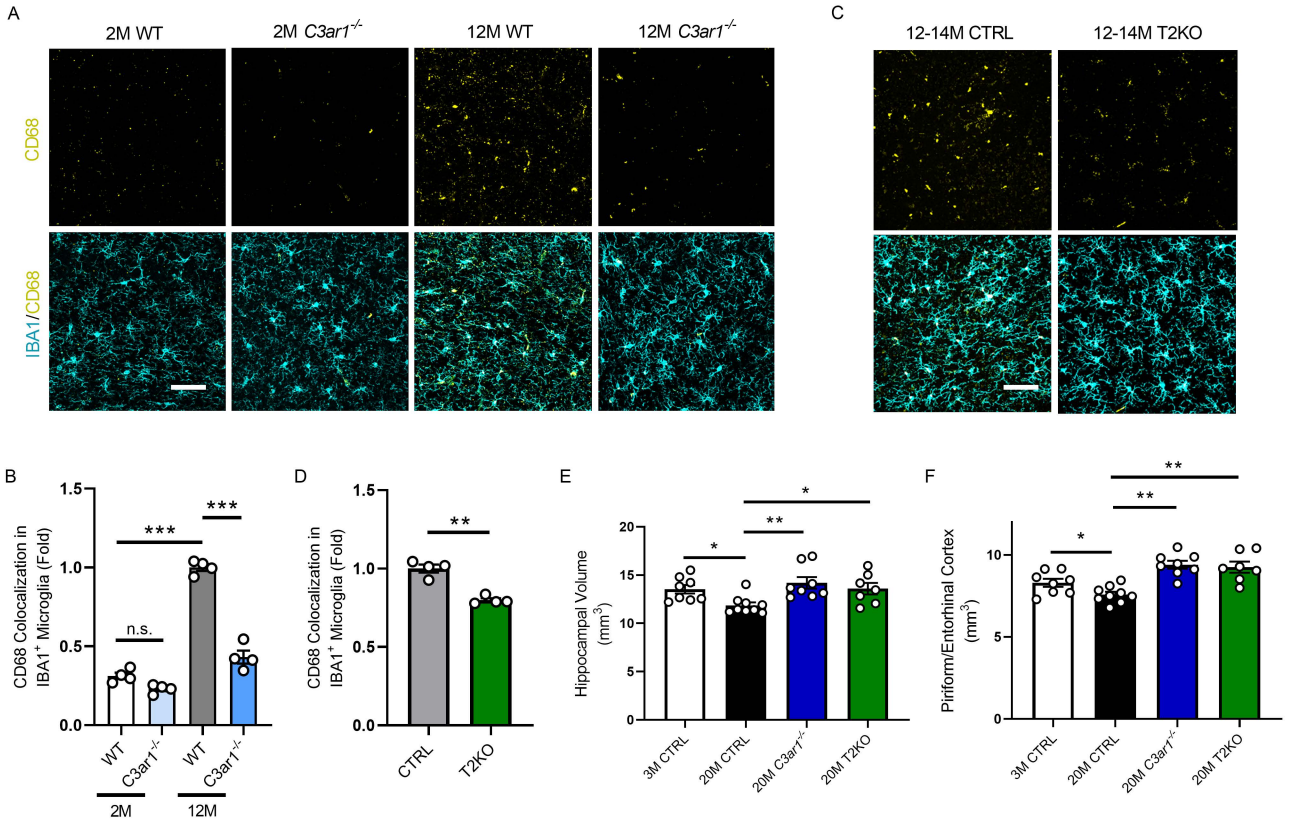
A
2M WT
2M C3ar1-/-
12M WT
12M C3ar1-/-
CD68
IBA1/CD68
C
12-14M CTRL
12-14M T2KO
B
CD68 Colocalization in IBA1+ Microglia (Fold)
1.5
1.0
0.5
0.0
***
***
n.s.
WT
C3ar1-/-
WT
C3ar1-/-
2M
12M
D
CD68 Colocalization in IBA1+ Microglia (Fold)
1.5
1.0
0.5
0.0
**
CTRL
T2KO
E
Hippocampal Volume (mm3)
20
15
10
5
0
*
**
*
3M CTRL
20M CTRL
20M C3ar1-/-
20M T2KO
F
Piriform/Entorhinal Cortex (mm3)
10
5
0
*
**
**
3M CTRL
20M CTRL
20M C3ar1-/-
20M T2KO

Figure 7. Germline and conditional knockout of *C3ar1* rescues age-related microglial reactivity and neurodegenerative phenotypes. (A) Representative IBA1 and CD68 double immunostaining in WT and *C3ar1*$^{-/-}$ hippocampus at 2M and 12M. **(B)** Quantification of CD68 immunoreactivity within IBA1^{+} microglia (n=4/group). **(C)** Representative IBA1 and CD68 double immunostaining in CTRL and T2KO hippocampus at 3M and 12-14M. **(D)** Quantification of CD68 immunoreactivity within IBA1^{+} microglia (n=4/group). **(E)** Quantification of hippocampal volume through coronal, serially sectioned tissue samples (n=7-9/group, 9 sections/animal quantified). **(F)** Quantification of entorhinal cortex volume through coronal, serially sectioned tissue samples (n=7-9/group, 9 sections/animal quantified). Data for (B) and (E) are means ± SEM and analysis was performed using one-way ANOVA with Tukey's post hoc test (*p <.05, **p<.01, ***p<.001). n.s.: not significant. Data for (D) are means ± SEM and analysis was performed using a two-tailed student's t-test (**p<.01). Data for (F) are means ± SEM and analysis was performed using one-way ANOVA with Holm-Sidak's post hoc test (*p <.05, **p<.01). Scale bar (A) and (C) = 50 μm.

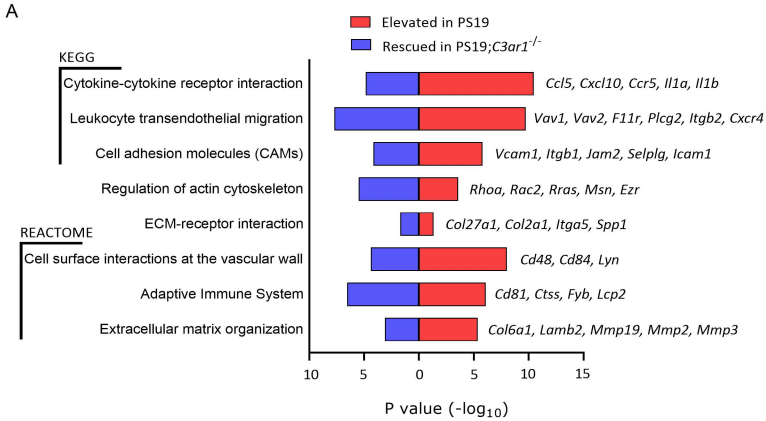
A
Elevated in PS19
Rescued in PS19;C3ar1-/-
KEGG
Cytokine-cytokine receptor interaction
Ccl5, Cxcl10, Ccr5, Il1a, Il1b
Leukocyte transendothelial migration
Vav1, Vav2, F11r, Plcg2, Itgb2, Cxcr4
Cell adhesion molecules (CAMs)
Vcam1, Itgb1, Jam2, Selplg, Icam1
Regulation of actin cytoskeleton
Rhoa, Rac2, Rras, Msn, Ezr
ECM-receptor interaction
Col27a1, Col2a1, Itga5, Spp1
REACTOME
Cell surface interactions at the vascular wall
Cd48, Cd84, Lyn
Adaptive Immune System
Cd81, Ctss, Fyb, Lcp2
Extracellular matrix organization
Col6a1, Lamb2, Mmp19, Mmp2, Mmp3
10 5 0 5 10 15
P value (-log10)

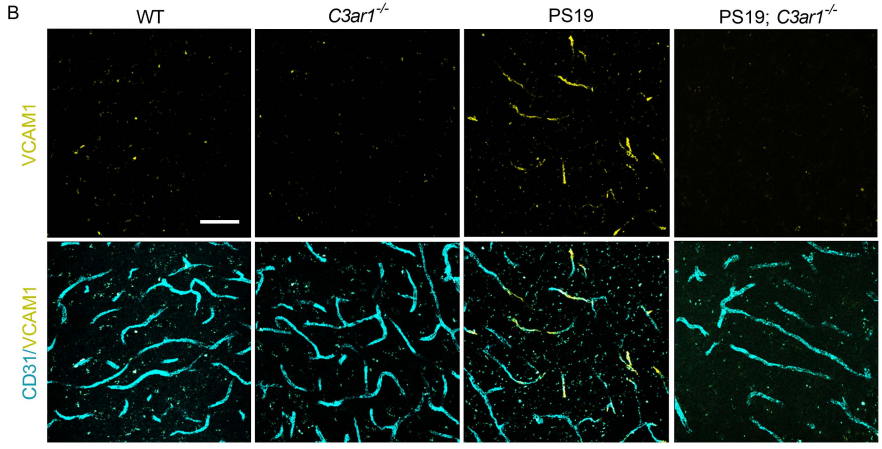
B
WT
C3ar1-/-
PS19
PS19; C3ar1-/-
VCAM1
CD31/VCAM1

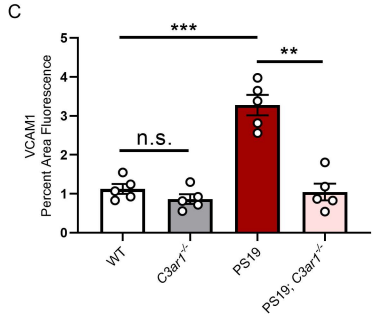
C
***
**
n.s.
VCAM1
Percent Area Fluorescence
0 1 2 3 4 5
WT
C3ar1-/-
PS19
PS19; C3ar1-/-

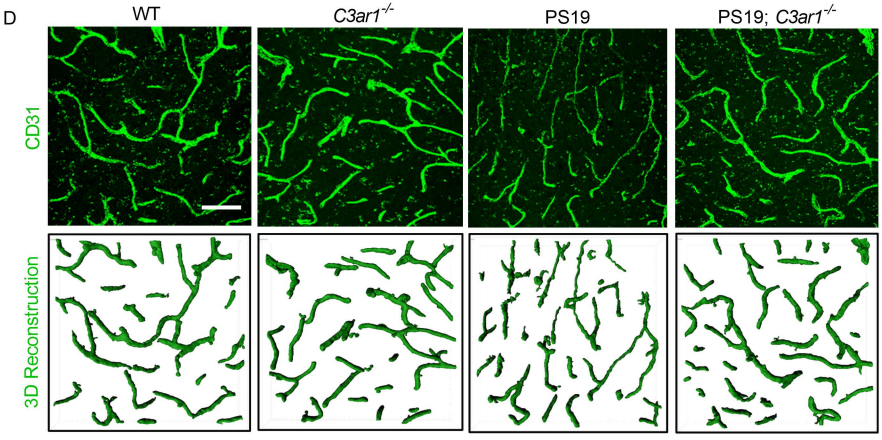
D
WT
C3ar1-/-
PS19
PS19; C3ar1-/-
CD31
3D Reconstruction

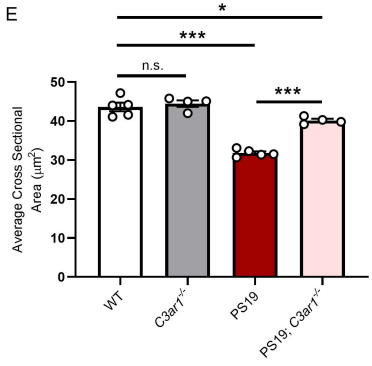
E
*
***
n.s.
***
Average Cross Sectional Area (μm2)
0 10 20 30 40 50
WT
C3ar1-/-
PS19
PS19; C3ar1-/-

Figure 8. Vascular abnormalities in PS19 tau transgenic mice and C3aR-dependency. (A) RNA-seq analysis revealed significantly overrepresented pathways in the DEGs that were increased in 9 month-old PS19 compared to wild-type animals (red), and that were decreased in PS19;*C3ar1*$^{-/-}$ compared to PS19 animals (blue). Terms were selected from results based on their involvement in vascular biology and immune cell infiltration, plotted by p value, and representative rescued genes contributing to the terms are listed (right). **(B)** Cortical staining of 9 month-old WT, *C3ar1*$^{-/-}$, PS19, and PS19;*C3ar1*$^{-/-}$ hippocampal vasculature with CD31 and VCAM1 demonstrate a significant increase in VCAM1 expression in PS19 mice, and a rescue of this phenotype in PS19 mice harboring *C3ar1* deletion. **(C)** Quantification of VCAM1 immuno-intensity. **(D)** CD31 staining and IMARIS-aided 3D reconstruction of 9 month-old WT, *C3ar1*$^{-/-}$, PS19, and PS19;*C3ar1*$^{-/-}$ hippocampal vasculature. **(E)** Quantification of average vessel cross-sectional area. All data are means ± SEM of n=5/group. Analysis for all results was performed using one-way ANOVA with Tukey's post hoc test (*p <.05, **p<.01, ***p<.001). n.s.: not significant. Scale bar = 50 μm.